SYNTHESIS AND CHARACTERIZATION OF PLASTIC SCINTILLATOR SAMPLES WITH DIFFERENT ADDITIVES

by

Mustafa Kandemir

B.S., Physics, Boğaziçi University, 2023

Submitted to the Institute for Graduate Studies in
Science and Engineering in partial fulfillment of
the requirements for the degree of
Master of Science

Graduate Program in Physics

Boğaziçi University

2025

ACKNOWLEDGEMENTS

Foremost, I would like to express my deep gratitude to my advisor, Bora Akgün, for providing this great opportunity and for being a close mentor throughout this work.

I sincerely thank Prof. Sertaç Öztürk for making this study possible and welcoming us to Scintillator Detectors R&D Laboratory at İstinye University. I am also truly grateful to Yağızhan Şahin, Zeynep Akbulut and Cengizhan Koyutürk, who put tremendous effort into this project.

Finally, I would like to thank my mother for always being there and supporting me, especially when things were at their worst.

This work was supported by TÜBİTAK (118C223, 122F271, 2211152) and by the Directorate of Presidential Strategy and Budget of Türkiye (2009K120520).

ABSTRACT

SYNTHESIS AND CHARACTERIZATION OF PLASTIC SCINTILLATOR SAMPLES WITH DIFFERENT ADDITIVES

Plastic scintillators are commonly used in radiation detection due to their low cost, mechanical robustness, and ease of fabrication. This thesis presents two complementary studies on plastic scintillator synthesis: optimization of fluor composition and concentration, and investigation of polymerization conditions through characterization of optical properties. All samples were produced by thermal polymerization.

To study the fluor loading, three different samples (CR-1, CR-2 and CR-3) were synthesized and characterized through their transmission spectra, emission distributions and light-yields. Their optical properties are found to be comparable to a high-light-yield EJ-204 reference sample.

The effects of polymerization initiators were investigated by synthesizing five different samples. The samples were produced using two commonly employed polymerization initiators, 2,2-Azobis(2-methylpropionitrile) (AIBN) and benzoyl peroxide (BPO) at concentrations of 0.2%, 0.5%, 1.0%. light-yield was evaluated relative to a control sample prepared without initiator, using four gamma sources and Compton edge analysis. Higher initiator concentrations consistently reduced light output: 0.2% initiator loading limited the reduction to approximately 8%, whereas 0.5–1.0% loadings decreased the yield by 20–35%.

The results provide practical guidelines to balance fluor composition, concentration and use of polymerization initiator in plastic scintillator synthesis.

ÖZET

ÇEŞİTLİ KATKI MADDELERİYLE SENTEZLENEN PLASTİK SİNTİLATÖR ÖRNEKLERİNİN KARAKTERİZASYONU

Plastik sintilatörler düşük maliyetleri, mekanik sağlamlıkları ve kolay üretilebilir olmaları nedeniyle radyasyon tespitinde yaygın olarak kullanılmaktadır. Bu tez, plastik sintilatör sentezi ile ilgili iki çalışmayı sunmaktadır: flor bileşimi ve derişiminin optimize edilmesi ile polimerizasyon koşullarının optik özelliklerin karakterizasyonu üzerinden incelenmesi. Tüm sintilatör örnekleri termal polimerizasyon yöntemi ile üretilmiştir.

Flor katkısının etkilerini incelemek için üç farklı sintilatör örneği (CR-1, CR-2, CR-3) sentezlenmiş ve bu örnekler spektral geçirgenlikleri, emisyon dağılımları ile ışık verimlilikleri üzerinden karakterize edilmiştir. Sentezlenen örneklerin optik özellikleri, yüksek ışık verimli EJ-204 referans sintilatörüyle karşılaştırılabilir bulunmuştur.

Polimerizasyon başlatıcılarının etkilerini araştırmak için beş farklı örnek sentezlenmiştir. Bu örnekler, farklı derişimlerde iki polimerizasyon başlatıcı -2,2-Azobis(2-methylpropionitrile) (AIBN) ve benzoil peroksit (BPO)- kullanılarak hazırlanmıştır. Işık verimi, polimerizasyon başlatıcı içermeyen kontrol örneğine göre dört farklı gama kaynağı kullanarak ve Compton spektrumu analizi ile değerlendirilmiştir. Polimerizasyon başlatıcı derişimini artmasının, ışık verimini düşürdüğü gözlemlenmiştir.

Elde edilen sonuçlar, plastik sintillatör sentezinde flor bileşimi, flor derişimi ve polimerizasyon başlatıcı kullanımının dengelenmesine yönelik yönergeler sunmaktadır.

TABLE OF CONTENTS

LIST OF FIGURES

LIST OF TABLES

LIST OF SYMBOLS

A	Mass number (atomic mass)
Z	Atomic number
Z_{eff}	Effective atomic number
N_A	Avogadro's number
r_e	Classical electron radius
m_e	Electron rest mass
c	Speed of light in vacuum
E	Energy
E_i	Incident photon energy
E_e	Kinetic energy of the recoil electron
CE	Compton edge position in the spectrum
RLY	Relative light yield
G	Photomultiplier tube gain
ρ	Density of the material
β	Relativistic velocity parameter, $\beta = v/c$
γ	Lorentz factor, $\gamma = (1 - \beta^2)^{-1/2}$
$\delta(\beta\gamma)$	Density-effect correction term in the Bethe–Bloch formula
θ	Photon scattering angle in Compton scattering
φ	Recoil electron scattering angle in Compton scattering

LIST OF ACRONYMS/ABBREVIATIONS

APD	Avalanche Photodiode
Bis-MSB	1,4-Bis(2-methylstyryl)benzene
CE	Compton Edge
FRET	Förster Resonance Energy Transfer
keV	kiloelectron volt
LY	Light-yield
MeV	megaelectron volt
PMT	Photomultiplier Tube
PDE	Photon Detection Efficiency
POPOP	1,4-Bis(5-phenyl-2-oxazolyl)benzene
PPO	2,5-Diphenyloxazole
PTP	p-Terphenyl
RLY	Relative Light Yield
SiPM	Silicon Photomultiplier
SPAD	Single Avalanche Photodiode
UV	ultraviolet

1. INTRODUCTION

Ionizing radiation is the energy emitted from a radioactive source as charged particles (e.g., beta and alpha particles) or indirectly induced ionization by neutral particles (e.g., neutrons, gamma-rays, and X-rays). Sensitive detection of ionizing radiation is essential across various fields, from medical imaging [1, 2] (such as PET scans and X-ray imaging) to nuclear reactor monitoring [3].

Ionizing radiation detection is also the backbone of modern high- and low-energy physics experiments. In high-energy experiments, enormous numbers of photons, electrons, and hadrons are produced with high energies; therefore, it is essential to distinguish among them [4, 5]. In low-energy experiments, such as direct dark matter detection [6, 7], low-energy photon detection [8], and rare event experiments [9], it is critical to suppress the background noise in order to detect weak signals.

Ionizing radiation can be detected with gas-filled ionization devices, semiconductor sensors, and scintillators. A scintillator first converts the ionizing event into visible or near-visible photons, which are then recorded by a photodetector. Although semiconductor sensors generally offer a better energy resolution than scintillator systems [10], cooling requirements and the high material cost make them impractical to use in large sizes.

Scintillating detector systems can be made in almost any size, from millimeter-thick fibers [11] to a total area of hundreds of square meters, as in the plastic tile calorimeter in the CMS experiment at CERN [12]. The most commonly used photodetectors for scintillators, such as photomultiplier tubes, avalanche photodiodes, and silicon photomultipliers, all rely on the photoelectric effect to generate charge. Due to their photocathode or semiconductor band-gap, these devices are most efficient in the visible and ultraviolet (UV) regions of the electromagnetic spectrum [13–15].

Scintillating detector systems can employ inorganic crystals [16], organic single crystals [17], noble gas or liquid media [18], and plastic scintillators [19] as the light-emitting material. Among these choices, plastic scintillators are commonly preferred in radiation detection as they are easy to machine into almost any shape, mechanically durable, tolerant of high counting rates, and cost-effective. However, plastic scintillators also have certain limitations. For instance, they exhibit a moderate light-yield (LY) compared to inorganic scintillators and organic crystals [20–22]. Additionally, because of their low effective atomic number, plastic scintillators typically do not exhibit a photopeak, unless sensitized with high-Z additives [22], which limits their suitability for applications requiring high energy resolution.

A widely accepted synthesis approach of plastic scintillators is thermal polymerization, which requires heating the monomer-additive mixture until it converts to a polymer. Optimizing the synthesis procedure of plastic scintillators is essential. This optimization includes determining the type and concentration of constituents, as well as the conditions applied during the polymerization process.

Chapter 2 introduces related theoretical background relevant to the conducted studies. Chapter 3 covers the methods used in synthesis of plastic scintillator samples, a general overview of the experimental setup and data acquisition, and the methodology of the light-yield calculations. Chapter 4 presents the synthesis and the characterization of plastic scintillator samples with different fluor compositions and concentrations. Chapter 5 examines the effects of polymerization initiators on the light output of the synthesized plastic scintillator samples. Finally, Chapter 6 summarizes the main findings and concludes the thesis.

2. THEORY

This chapter will explore types of radiation, detection principles, photodetectors, inorganic and organic scintillation processes. Section 2.5 details the scintillation process and characteristics of plastic scintillators, as Chapter 4 and Chapter 5 explore synthesis and characterization of them.

2.1. Types of Radiation

Radiation is energy that is emitted from a radioactive source as particles or waves. It can be divided and investigated into four main subgroups: heavy charged particles, beta particles, neutrons, and electromagnetic waves. Each group originates from various sources and possesses different attributes. Having distinct properties, detection of different radiation types generally requires different approaches.

2.1.1. Heavy Charged Particles

Heavy unstable nuclei undergo alpha decay, producing alpha particles. Commonly utilized alpha sources, ^{241}Am, ^{210}Po, and ^{226}Ra, have diverse half-lives from days to thousands of years. However, the emitted alpha particles have similar energies, in the $4-6$ MeV range. The energy of the alpha particle and the half-life of the source are closely related; alpha particles with more than 6.5 MeV energy have half-lives that are too short for practical purposes [23]. Heavy charged particles (i.e., protons, heavy ions, and alpha particles) can be created artificially in nuclear reactors and accelerators; the latter offers the opportunity to adjust the energy and propagation direction as required by the application [24–26].

A charged particle leaves a trace of ionization as it moves through a medium. Energy is dissipated primarily by inelastic collisions with electrons. Charged particles follow mostly straight paths except for nuclear collisions, which are very rare. Energy

dissipated in the medium is calculated by the Bethe-Bloch formula, by integrating the stopping power $\mathrm{d}E/\mathrm{d}r$. The Bethe-Bloch formula is expressed as,

$$-\frac{\mathrm{d}E}{\mathrm{d}r} = \frac{4\pi N_A r_e^2 m_e c^2}{\beta^2}\,\frac{Z}{A}\,z^2\left[\ln\left(\frac{2m_e c^2\beta^2\gamma^2}{I}\right) - \beta^2 - \frac{\delta(\beta\gamma)}{2}\right], \tag{2.1}$$

where N_A is Avogadro's number, r_e is the classical electron radius, m_e the electron mass, c is the speed of light, Z and A are the atomic number and mass of the absorber, z is the charge of the incident particle in units of e, I is the mean excitation potential, $\delta(\beta\gamma)$ is the density-effect correction, and β and γ are the usual relativistic factors. Equation (2.1) was introduced by Bethe [27], quantum relativistic corrections were made by Bloch [28] and the density-effect correction is calculated by Sternheimer [29]. This relation is valid for velocities $0.1 \lesssim \beta\gamma$. At low energies, particles slow down enough to capture electrons, effectively become neutralized, and lose their capability to ionize further.

The Bragg-Kleeman rule, an empirical relation, is a useful identity that compares the range of a charged particle in a material with that of another reference material. The relation is expressed as,

$$\frac{r_1}{r_0} = \frac{\rho_0\sqrt{A_1}}{\rho_1\sqrt{A_0}} \tag{2.2}$$

where r_i is range of the particle, ρ_i is density and A_i is atomic weight of the material. For compounds, the effective atomic weight can be calculated by

$$\sqrt{A} = \frac{n_1A_1 + n_2A_2 + ...}{n_1\sqrt{A_1} + n_2\sqrt{A_2} + ...} \tag{2.3}$$

where n_i is the atomic fraction of the constituent element of atomic weight A_i. Choosing reference medium as air, $\sqrt{A_0} = 3.82$, $\rho_0 = 1.226 \times 10^{-3}\mathrm{gcm}^{-3}$ at 15°C, 760 mmHg Bragg-Kleeman rule becomes

$$r = 3.2 \times 10^{-4}\frac{\sqrt{A}}{\rho}r_{Air}. \tag{2.4}$$

A detailed calculation and a table of parameters for widely used detector materials can be found in Birks' works [30]. This equation is quite useful in detector design [31].

2.1.2. Electrons

Common methods of producing electrons involve beta decays, internal conversion, and the Auger effect. In beta decay, a nucleon transforms into its isospin partner. There are two different types of beta decay named according to charges of the emitted particle; β^- produces an electron and an antineutrino, while β^+ produces a positron and a neutrino. Q-value is shared between emitted particles and the recoiling daughter nucleus, resulting in a continuous energy spectrum. For many beta sources, the daughter nucleus is left in an excited state, which subsequently decays by emitting electromagnetic radiation. Pure beta sources, those that only emit beta particles with no accompanying electromagnetic radiation, do exist, but they are relatively rare [23]. Since the kinetic energy is shared between the daughter nuclei, the electron, the neutrino, and the electromagnetic radiation, beta decays do not produce monoenergetic electrons.

An illustration of ^{137}Cs β-particle energy is shown in Figure 2.1a. The figure illustrates the relative yield of beta particles at different energy values. In the most probable case, the electrons have an energy around 0.2 MeV, whereas the maximum kinetically allowed energy for this decay is 0.714 MeV. The gamma-ray energies, branching ratios, and half-lives used in this work are taken from the ENSDF evaluations as compiled in the NNDC NuDat 3 database [32], unless stated otherwise.

Internal conversion produces practically monoenergetic electrons. The process begins with an excited nucleus. Instead of emitting a photon, the nucleus transfers its excitation energy directly to an inner shell electron, ejecting it. The kinetic energy of the emitted electron is equal to the difference between the nuclear transition energy and the electron's binding energy.

In the Auger effect, a preceding event (such as electron capture or the photoelectric effect) creates a vacancy in an inner electron shell. A higher shell electron fills in this vacancy, and the released energy is transferred directly to another electron, caus-

ing it to be ejected without photon emission. The most energetic photons are released when conversions take place in the innermost shells, the K-shell and the L-shell. The Auger effect primarily occurs in light atoms where electron binding energies are small. Auger electrons thus have a discrete energy spectrum. While beta decay and internal conversion generally produce fast electrons with energies ranging from hundreds of keV to a few MeV, Auger electrons are typically slow, having energies of a few keV [33]. Figure 2.1b depicts internal conversion spectrum of ^{137}Cs to ^{136m}Ba. The innermost shell conversions in this decay produce electrons of 365 keV energy, whereas L-shell conversion produces higher-energy electrons with 389 keV energy.

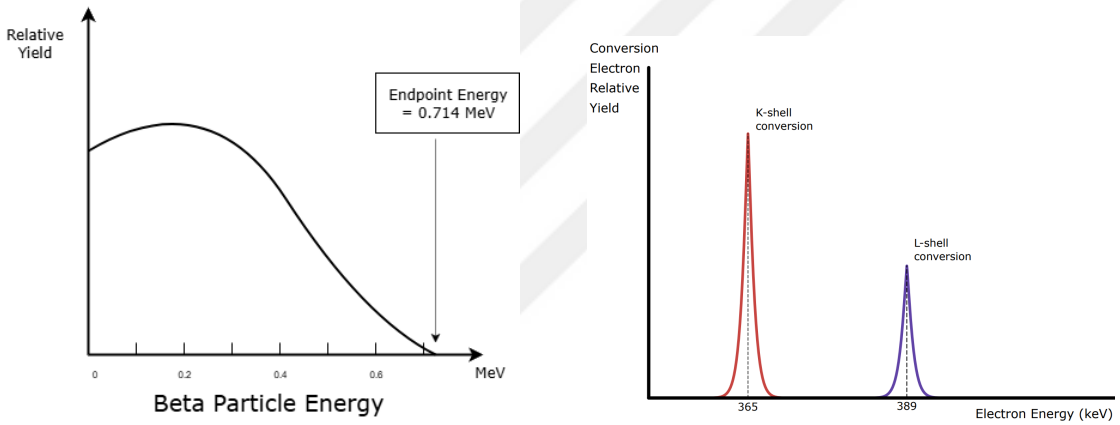

(a) (b)

Figure 2.1. (a) Beta Spectrum; (b) Internal Conversion Spectrum.

When passing through a medium, electrons dissipate their energy by ionization, excitation, scattering off nuclei, and radiation (Bremsstrahlung). Radiative energy loss becomes significant only at higher electron energies. In lead, radiative and ionization energy losses become comparable at electron energies around 9 MeV, for water and air, this value is around 100 MeV [30].

Contrary to heavy charged particles, electrons do not move in straight trajectories; instead follow winding paths. Because electron trajectories are irregular, the concept of range differs from that of heavy charged particles. The practical range of an electron in a medium is defined empirically as the absorber thickness required to stop

most of the electrons. Consequently, electron ranges are calculated statistically rather than as sharply defined penetration depths.

2.1.3. Neutrons

There are no natural neutron sources that are of practical use. Nuclei that emit neutrons via spontaneous fission exist, but they have extremely long half-lives and very low spontaneous fission rates. For example, ^{238}U has a half-life around 4.5 billion years and undergoes one spontaneous fission reaction for every 2×10^6 alpha emission [34]. However, several mechanisms exist to produce neutrons artificially, including the use of accelerated protons or high-energy gamma-rays to eject neutrons from target nuclei.

Spallation is one such technique that utilizes accelerated protons to eject neutrons. Neutrons produced by this method have a broad energy range, from fractions of an eV to several hundred MeV. In photoneutron production, gamma-rays interact with nuclei, causing the emission of neutrons with energies typically ranging from a few hundred keV to several MeV [35].

Another important neutron source is ^{252}Cf, which does not occur naturally. The production depends on irradiation of heavy elements, such as americium, plutonium and curium. Target elements undergoes series of neutron captures and β-decays [36]. This chain of processes requires high-flux reactors, therefore very limited number of facilities can produce the isotope [37]. ^{252}Cf has a half-life of 2.645 years [38] and a very high neutron emission rate. These characteristics, along with its portability, make it the standard commercial neutron source.

Neutrons, being electrically neutral, cannot be directly detected through ionization. Secondary products, charged particles or electromagnetic radiation, emitted from neutron-matter interactions, play a key role in neutron detection. Neutrons pass through the electron cloud of an atom and directly interact with the nucleus.

Fast neutrons interact with the nuclei primarily through scattering events, transferring a portion of their energy to recoil nuclei. Hydrogen is an ideal target for fast neutron detection due to its comparable mass to the neutron, which allows efficient energy transfer. Slow neutrons are typically captured by nuclei, forming heavier, often excited isotopes. These nuclei emit high-energy gamma-rays, enabling indirect detection [39].

2.1.4. Electromagnetic Radiation

In the electromagnetic spectrum, only X-rays and gamma-rays have enough energy to be defined as ionizing radiations. X-rays are naturally produced by electron transitions between inner atomic shells. When an inner-shell electron is ionized, an outer-shell electron fills the empty shell, releasing a photon with energy equal to the difference between the shell binding energies. Light atoms emit photons with energies of a few hundred eV, while heavier atoms, due to their higher Coulomb potential and stronger binding energies, produce photons with energies on the order of tens of keV [40].

Bremsstrahlung is another process of X-ray production. When a moving charged particle is affected by another charged particle, generally by a nucleus, it may change direction and decelerate, losing some of its kinetic energy. This kinetic energy is released as photons, forming a continuous spectrum of X-rays. Bremsstrahlung radiation is formed when the acceleration of the particle is along its velocity vector. If a particle is accelerated perpendicular to its velocity by a magnetic field, it releases electromagnetic radiation called synchrotron radiation. Circular accelerators use magnetic fields to bend the paths of charged particles, inevitably producing synchrotron radiation as a byproduct. This radiation spans wavelengths from visible light [41] up to the X-ray range [42].

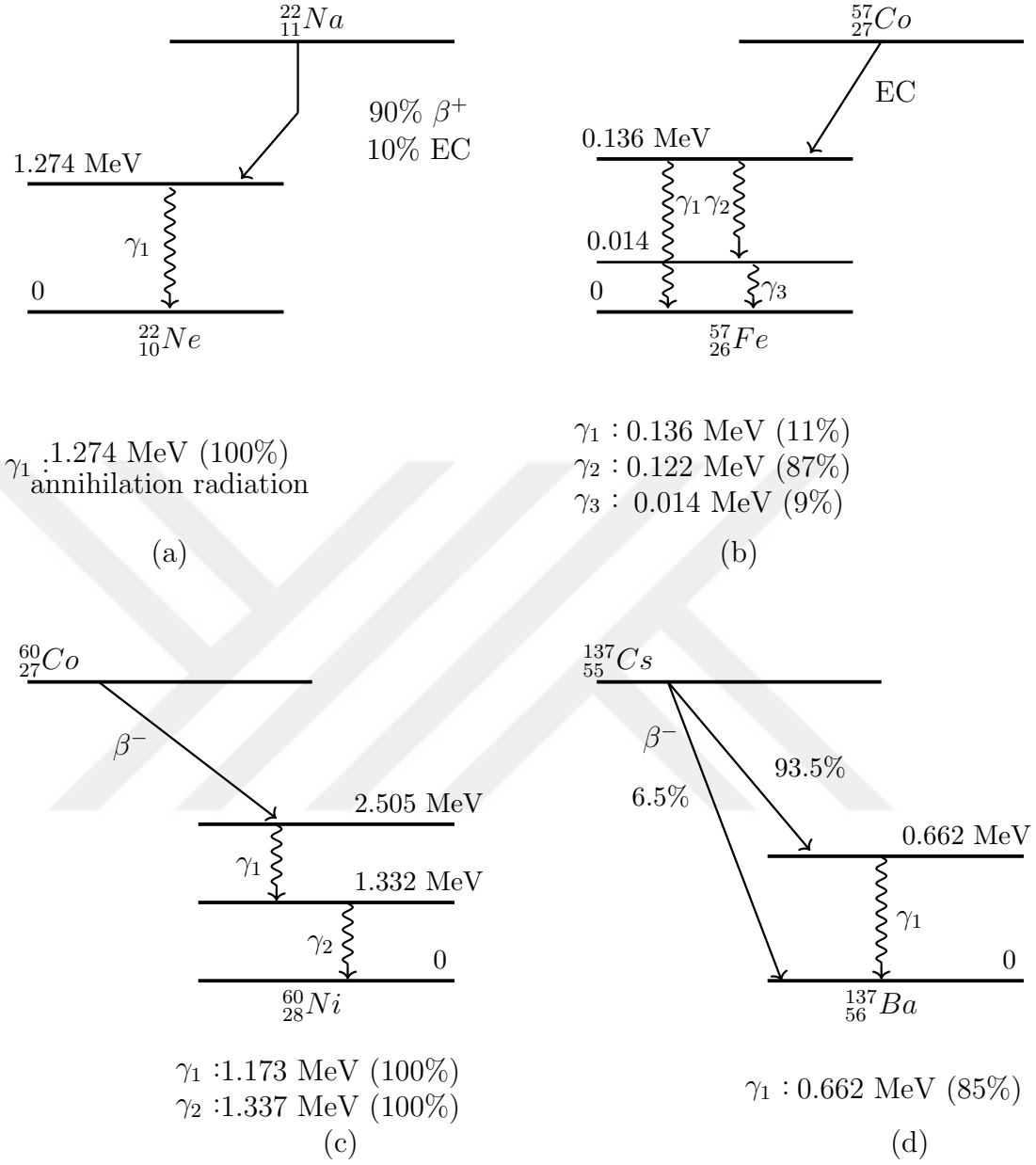

Figure 2.2. Decay schemes of common gamma sources; (a) $^{22}_{11}Na$, (b) $^{57}_{27}Co$, (c) $^{60}_{27}Co$, and (d) $^{137}_{55}Cs$.

Natural formation of gamma-rays generally follows nuclear processes. Nuclear reactions such as neutron capture, fission, fusion, and beta decay produce gamma-rays emitted at discrete energies corresponding to the differences between nuclear energy levels [43]. In particular, gamma-rays that follow β decay are preferred as laboratory sources because the parent nuclei can be sealed for long periods and require only moderate shielding.

In a typical decay, the parent nucleus emits a β particle, leaving the daughter in an excited state; subsequently, the daughter nucleus de-excites by emitting one or more gamma-rays. As shown in Figure 2.2d, ^{137}Cs emits a β^- particle and transforms into ^{137m}Ba, which is a metastable isotope of barium. Then ^{137m}Ba emits a gamma-ray of energy 0.662 MeV and becomes stable. Figure 2.2c depicts the similar process for ^{60}Co. It undergoes β^- decay and populates an excited state of ^{60}Ni, which emits two distinct photons of energy 1.173 and 1.332 MeV.

For β^+ emitters, the emitted positron annihilates with an electron in the surrounding medium, which produces a pair of photons with energies of 0.511 MeV traveling opposite directions. As shown in Figure 2.2a, ^{22}Na experiences β^+ decay or electron capture and transforms into an excited state of ^{22}Ne, which radiates a gamma-ray of energy 1.274 MeV. The favored reaction, with 90% branching ratio, β^+ decay also produces annihilation photons. Therefore, the spectrum of ^{22}Na contains two discrete gamma-ray lines. The decay schemes of the aforementioned nuclides are shown in Figure 2.2b shows the decay process of ^{57}Co. It undergoes an electron capture and decays into an excited state of ^{57}Fe, from which three different photon emissions, with energies of 0.136, 0.122, and 0.014 MeV, are possible.

2.2. Detection Principles

Detection is the process of converting radiation into a measurable signal so that a human can comprehend, analyze, and work with it. This could be a kind of visible light, some paths drawn on some type of paper, or more generally and contemporarily, an electric signal which will then be transformed into some numbers so that it can be compared to relevant others.

Detection requires that ionizing radiation transfer some or all of its energy to a detector medium. Charged particles primarily lose their energy by ionizing the medium directly. In contrast, neutral particles, such as neutrons and electromagnetic radiation,

must first undergo specific interactions within the medium to produce detectable secondary particles.

Neutrons interact predominantly with atomic nuclei. Through scattering or absorption processes, their kinetic energy is transferred to nuclei, which then emit charged particles or photons as secondaries that can be detected. The kinetic energy transferred to the target nuclei increases as their mass lowers and becomes comparable to that of a neutron. Therefore, hydrogen plays a crucial role in neutron detection.

Electromagnetic radiation may undergo various types of interactions, three of which are essential for detection: the photoelectric effect, Compton scattering, and pair production.

In the photoelectric effect, a photon transfers all of its energy to a bound electron, ejecting it from the atom. The electron gains kinetic energy that is equal to the difference between the energy of the photon and the binding energy. This electron may be detected directly, or it may initiate further ionization, amplifying the detectable signal.

Another important photon-electron interaction is Compton scattering. The interaction is modeled as an elastic collision between a photon and an essentially free electron as depicted in Figure 2.3. In Compton scattering, the photon transfers only a portion of its energy to the electron, resulting in a continuous spectrum.

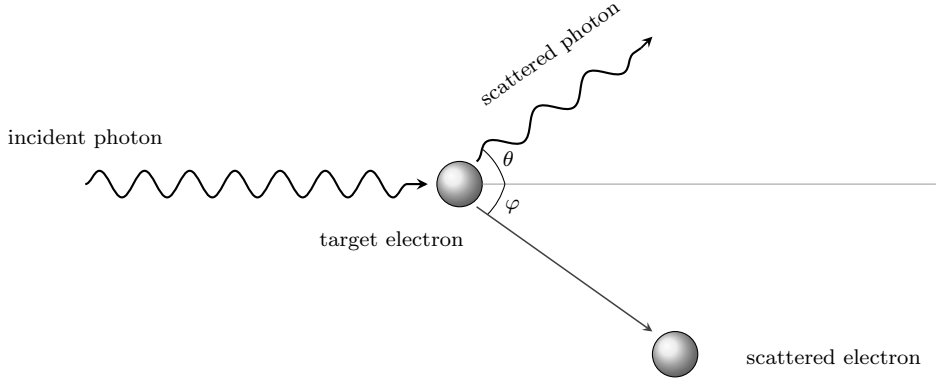

Figure 2.3. Compton Scattering.

Let us assume a photon of initial energy E_i interacts with a stationary electron. After the interaction, the photon scatters with an angle θ and energy E_f, the electron scatters with an angle φ and energy E_e. Following the conservation of energy, the angles are related as,

$$\cot\varphi = \left(1 + \frac{E_i}{m_e c^2}\right) \tan\frac{\theta}{2}. \tag{2.5}$$

The energy of the recoil electron is,

$$E_e = E_i - \frac{E_i}{1 + \frac{E_i}{m_e c^2}(1 - \cos\theta)}. \tag{2.6}$$

The Compton edge of the spectrum occurs when the electron gains the maximum possible energy, E_{max}, which occurs when the photon scatters back, $\theta = \pi$, then the recoil electron has the energy,

$$E_{max} = \frac{2E_i^2}{2E_i + m_e c^2}. \tag{2.7}$$

The third important interaction of photon detection is pair production. This phenomenon occurs basically when a photon has enough energy to convert into an electron-positron pair. As in nearly all physics-related processes, the total energy of the system must be conserved. Therefore, the photon must at least have the rest mass energies of the electron-positron pair, that is $2m_0c^2 = 1.022MeV$. The photon may have more energy; the surplus energy is then distributed between the electron and the positron in kinetic form.

2.3. Photodetectors

Certain detectors are designed to use different detection principles to convert electromagnetic radiation into electrical signals. These devices initially convert photons into electrons and start a chain of events that produces typically $10^5 - 10^6$ electrons per photon so that a signal can be detected. This multiplication factor is referred to as the gain. Devices can vary in size, working principle, robustness, and necessary operating conditions. The following sections will shortly explain two widely used photodetectors.

2.3.1. Photomultiplier Tube

A photomultiplier tube (PMT) mainly consists of a photocathode, dynodes, and an anode. All parts are enclosed by a vacuum envelope and operate at a bias voltage. Incoming photons interact with the photocathode, which is sensitive to certain ranges of wavelengths (depending on the material used), and eject electrons upon interaction. Then the photoelectron accelerates towards the first dynode and ejects secondary electrons; this procedure repeats several times, creating a cascade. At the end, a herd of electrons hits the anode plate and an analog signal is produced. Each dynode is connected to the circuit at a different point with an accompanying voltage divider resistor so that the voltage differs by steps, hence electrons keep accelerating. A schematic representation of the PMT workflow is provided in Figure 2.4.

A photo-sensitive detector is characterized by its photon detection efficiency (PDE) and spectral response. PDE is the probability that an incident photon produces a detectable signal. For PMT, it is the product of quantum and collection efficiencies. Quantum efficiency is defined as the ratio of the number of photoelectrons that are produced at the photocathode to the number of incident photons. Collection efficiency is expressed as the probability of the collection of the photoelectron by the first dynode. Both depend on the material that the photocathode is made of. Quantum efficiency also differs along the electromagnetic spectrum. Peak PDE of a typical PMT is around $15 - 45\%$ [44] and occurs at different wavelengths. In general, PMTs are sensitive to UV, visible, and near-infrared regions.

The second important property is the gain. For PMTs, it is defined as the ratio of the anode current to the photocathode current. Gain depends on the operating voltage of a PMT, and can be formulated as,

$$\frac{G_1}{G_2} = \left(\frac{V_1}{V_2}\right)^{\alpha N} \tag{2.8}$$

where G_1 and G_2 are gains at operating voltages V_1 and V_2 respectively, α is a coefficient indicating the dynode material and geometry and N is the number of dynodes. PMTs operate at on the order of 1000 V to achieve gains of $10^5 - 10^7$ [45].

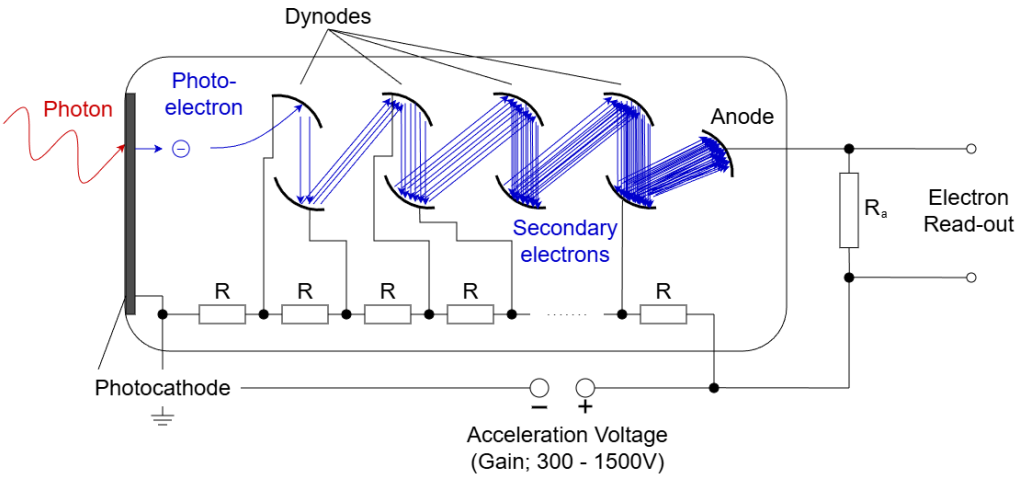

Figure 2.4. Schematic Diagram of PMT workflow.

PMTs are affected by temperature changes. The most common effects are a change in spectral response, gain, and anode sensitivity drift, and an increase in dark current with temperature. Even the heat generated internally may affect the results of delicate experiments. PMTs are also sensitive to magnetic fields; a weak magnetic field of the strength of Earth's magnetic field can affect the performance. As PMTs get larger, and the path electrons have to take gets longer, effects become more noticeable [46].

As PMTs are sensitive to visible light, any experiment must be conducted under a very dark environment. Depending on the size of the employed PMT, the use of a light-proof black box is suggested. A concise exploration of the historical development of PMTs has been provided by G. A. Morton [47], and is suggested for further reading.

2.3.2. Solid State Detectors

Solid-state detectors are another widespread type of radiation detector. Compared to vacuum-based detectors, they offer scalability, microfabrication, cost-efficiency, robustness, and less sensitivity to the magnetic field. Semiconductor detectors operate at lower voltages and achieve comparable gains as PMTs while possessing higher

quantum efficiencies. On the other hand, they have higher dark current per unit of photosensitive area and lower radiation hardness.

Semiconductors have moderate band gaps between their valence band and conduction band, lower than that of insulators but larger than conductors. If a semiconductor is doped with an element with an extra valence electron, *i.e.* group V elements such as phosphorus or arsenic, it turns into an n-type material. The extra electron acts as a free electron on the structure; therefore, the dopant is referred to as a donor impurity. Conversely, if a semiconductor is doped with a group III element such as boron or gallium, it turns into a p-type material. The three valence electron structure of the dopant creates a vacancy in the four-electron bonding structure of the semiconductor. This vacancy behaves as a hole, which can accept electrons, and the dopant is called an acceptor impurity.

When p-type and n-type materials meet, they form a junction. At this junction, electrons diffuse from the n-layer to the p-layer, and holes move from the p-layer to the n-layer. This process introduces a polarity around the junction. The initially neutral n-layer is now positively charged, and the p-layer is negatively charged. Around this junction, a depletion region is formed with a net electric field from the n-layer to the p-layer.

If a photon with energy equal to or larger than the band gap energy interacts with the semiconductor lattice, it creates electron-hole pairs. In the depletion region, these charge carriers move according to the electric field. When a change in the potential is measured, the incoming radiation is essentially detected.

In its most basic form, a p–n junction functions as a diode; when connected to a quenching resistor and operated under reverse bias, it becomes the simplest example of a solid-state detector. The reverse bias makes the detector more sensitive by widening the depletion region. It also creates a larger electric field in the depletion region, which enables faster collection of charge carriers. If a very high voltage, near break-

down voltage of the diode, is applied to this detector, the carriers are accelerated by the electric field between collisions and cause impact ionization, producing additional electron–hole pairs. This avalanche effect makes it possible to detect weaker signals with fewer initial carriers. This configuration produces a saturated, binary pulse independent of the number of primary carriers and therefore cannot resolve multiple simultaneous photons; hence, it is called single-photon avalanche diode (SPAD).

A primitive SPAD can be improved by inserting an intrinsic (i) layer to form a p–i–n (PIN) structure. A pure semiconductor intrinsic layer increases the depletion width and enables separate absorption and multiplication regions. Adding a quenching resistor terminates the discharge and sets the recovery time.

A large set of ($\sim 10^2 - 10^4\ mm^{-2}$ [48]) SPAD forms a silicon photomultiplier (SiPM). Each SPAD pixel operates at just above the breakdown voltage, in the so-called Geiger mode. Discharges from each pixel add up to an analog pulse. For a SiPM, PDE is defined as the product of quantum efficiency, avalanche probability, and fill factor (photosensitive area divided by total device area). A typical SiPM reaches a peak PDE comparable to PMTs, roughly 15–50%, depending on pixel size, wavelength, and operating voltage [49].

2.4. Scintillation

Both solid-state and vacuum-based detectors excel at detecting visible light and surrounding wavelengths. However, light-sensitive detectors are not capable of detecting alpha particles, beta particles, neutrons, gamma-rays, or X-rays. To employ these photodetectors, an intermediate component must convert ionizing radiation into visible light. The material responsible for this conversion is called a scintillator.

Scintillators are luminescent materials that absorb incoming ionizing radiation through scattering, absorption, photoelectric effect, Compton scattering, and inelastic collisions. The absorbed energy is then transferred non-radiatively within the medium

and emitted as visible light (or near UV) through either fluorescence or phosphorescence, depending on the material type. While both are luminescent, the key difference between fluorescence and phosphorescence is the decay time and the wavelength of the emitted light. Scintillators are typically categorized by their constituent materials as either organic or inorganic scintillators. Each type operates through distinct physical mechanisms that govern how the absorbed energy is converted into light.

2.4.1. Inorganic Scintillation

The crystal lattice structure of the inorganic scintillators dictates the scintillation mechanism. Inorganic scintillators are made of insulators and semiconducting materials, in which electrons can only fill discrete energy bands. The region in the lattice where electrons are bound is called the valence band, whereas the conduction band represents the areas where electrons are free to move. An excited electron can move from the valence band to the conduction band, undergo a de-excitation, and emit a photon. In pure crystals, this process is inefficient, and emitted photons are generally more energetic to lie in the visible spectra [23]. To obtain practical scintillators, crystals are doped with impurities, known as activators.

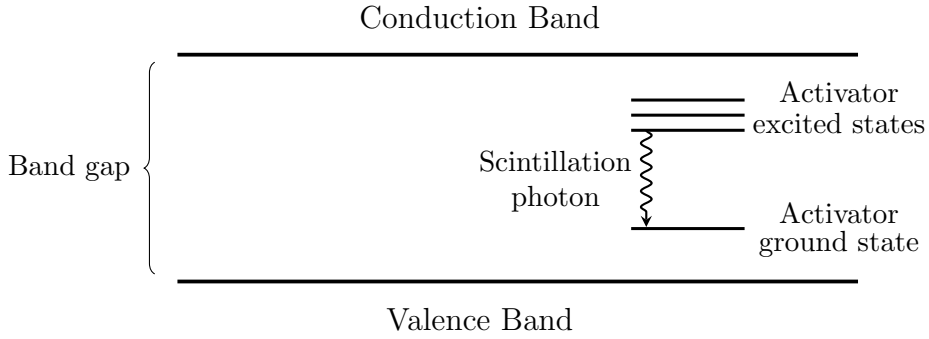

Figure 2.5. Energy band structure of an activated crystalline scintillator.

Figure 2.5 illustrates the energy band structure of an activated crystalline scintillator. Activators create intermediate energy states between the valence and the conduction bands. A modified band energy structure enables lower energy transitions, leading to more probable excitations and the creation of lower energy, visible-range

photons. The region of these new energy states determines the emission spectrum of the scintillator and is called the luminescence centers. Typical excitation time of the electrons is nearly instantaneous, on the order of picoseconds [50], and de-excitation can take up to hundreds of nanoseconds [51]. The phosphorescence occurs when the electron undergoes a transition to a state from which the de-excitation to the ground state is forbidden. In this case, the electron must be excited to a higher energy state, and it undergoes de-excitation to the ground state. The decay time of the phosphorescence can be on the order of seconds [52], which results in a late afterglow.

2.4.2. Organic Scintillation

In organic molecules, sp^2 hybridization results in p_z orbitals that overlap to form π-electron structure. π-electron structures have singlet and triplet energy levels.

Figure 2.6 depicts a schematic diagram of energy levels. The singlet states denoted as S_0, S_1, S_2, S_3 and the triplet states are denoted as T_1, T_2, T_3. S_0 and S_1 states are separated by 3-4 eV; the following are separated by lower energy differences. For each level, the triplet state is always less energetic than the singlet state. Double subscript states (S_{00}, S_{01}, S_{02}, S_{11}, S_{12}, S_{21}) represent the vibrational states, which have an approximate energy spacing of 0.1-0.2 eV. At thermal equilibrium at room temperature, higher energy vibrational states are less populated than the ground vibrational state (S_{00}), therefore electrons accumulate in S_{00}.

A scintillator is characterized by its efficiency. This efficiency is defined as the fraction of the emitted visible photon energy to the absorbed energy. A good scintillator should exhibit minimal energy loss during the scintillation process. Some organic molecules exhibit transitions that emit photons beyond the visible range, while others have non-radiative de-excitations. These energy losses are known as quenching.

Birks [30] classifies organic scintillators under three main categories: unitary systems, binary systems, and ternary systems. Unitary systems include pure organic

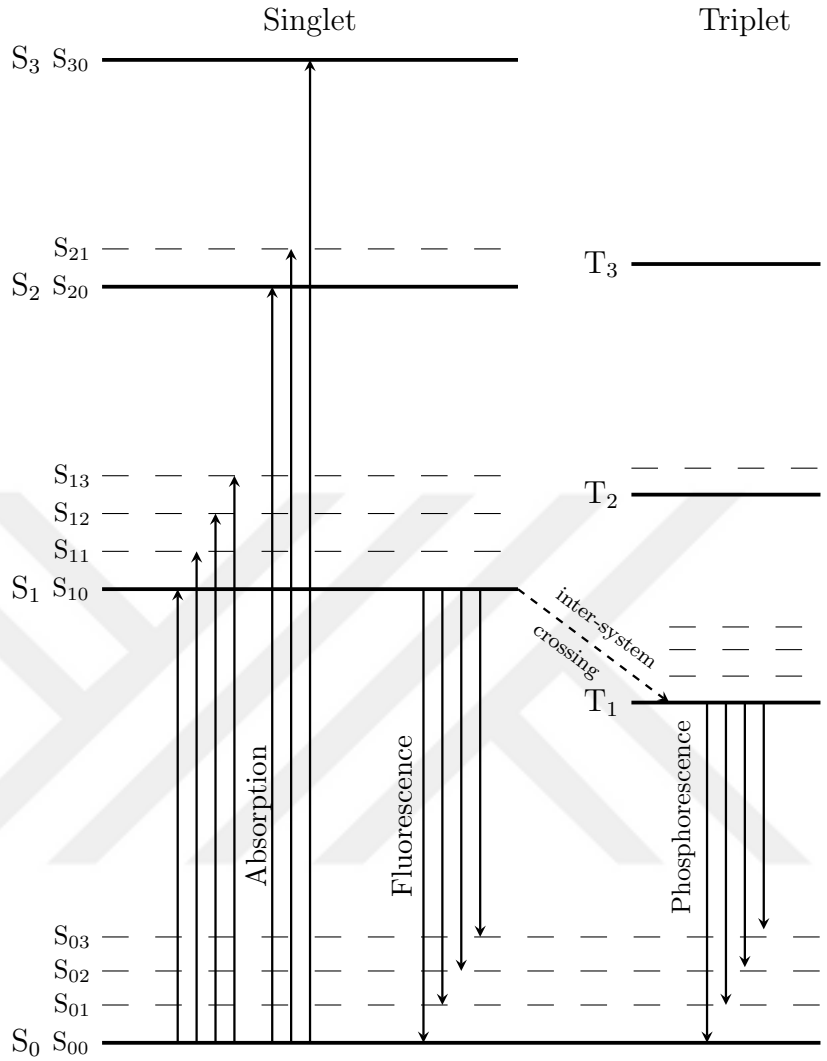

Figure 2.6. Schematic Jablonski diagram of an organic molecule with π-electron structure (after J. B. Birks [30]).

crystals, such as anthracene and stilbene. These crystals possess high scintillation efficiency. However, they are very fragile and of very limited sizes. Binary systems include two different agents, a solvent base, such as styrene and toluene, and a primary fluor, such as p-Terphenyl or a crystal. In such systems, the solvent base serves as the energy absorber and transfers energy to the primary fluor or crystals, which emit scintillation light. The ternary systems consist of a solvent base, a primary fluor, and a wavelength shifter. In some cases, the proportion of the primary fluor or the dimensions of the scintillator do not allow a sufficient conversion. The wavelength shifter absorbs the scintillation of the primary fluor and emits visible light. For special appli-

cations, scintillators are loaded with further additives. For instance, boron, lithium, and gadolinium are widely used to enhance neutron detection. Heavy-metal dopants such as lead, bismuth, or tantalum can be introduced to improve gamma-ray detection.

Binary and ternary organic scintillator systems can have either liquid or plastic forms. Liquid scintillators are the natural choice for applications that require very large volumes of scintillating materials, such as neutrino and anti-neutrino detections [53,54]. Since liquid scintillators lack a solid structure that can be degraded by radiation, they are more resistant to radiation damage than their solid counterparts. Dissolved oxygen in the solvent introduces a strong quenching effect for both liquid and plastic scintillators; therefore, it is important to remove the oxygen during the preparation process.

2.5. Plastic Scintillators

In this section, constituents, scintillation mechanism, and characteristics of ternary plastics scintillators will be discussed.

In essence, plastic scintillators are prepared with three different ingredients: a polymer matrix base, a primary fluor that is responsible for scintillation, and a secondary fluor to shift the wavelength to the desired interval. These three ingredients are prepared under strict circumstances to form plastic scintillators. The preparation process will be discussed in the next section.

2.5.1. Constituents and Scintillation Mechanism

The polymer base forms 70-97% [55] of a plastic scintillator by weight. Since ionizing radiation primarily interacts with the polymer base, it is responsible for the absorption and the transfer of excitation energy to the luminescence center. The polymer base also provides a solid structure to the scintillator. Therefore, it must be mechanically robust, optically transparent, and resistant to radiation damage. As machinability

is one of the major advantages of plastic scintillators, the material must be soft enough to be shaped into any desired geometry without compromising its structural integrity.

Polyvinyltoluene and polystyrene are the two most commonly employed aromatic polymer bases. Their π-$\pi*$ ring structure allows a non-radiative energy transfer through the scintillator. Figure 2.7 illustrates the Förster resonance energy transfer (FRET) mechanism, in which an excited donor molecule transfers its energy non-radiatively to an acceptor molecule through dipole–dipole coupling. The process was first described by Förster [56], from whom it takes its name.

These aromatic polymers, by themselves, can perform scintillation. However, their fluorescence lies in the near-UV region and they have a strong self-absorption. For efficient scintillation, the emission spectrum of the polymer base should overlap with the absorption spectrum of the primary fluor. Moreover, the polymer base should exhibit a high quantum efficiency, ensuring that a large fraction of the deposited energy is released as fluorescence rather than lost as heat.

The primary fluor absorbs the UV radiation that is emitted from the polymer base and emits visible light. Figure 2.8 illustrates the absorption and emission spectra of these compounds. Undergoing the same physical phenomena for luminescence, primary fluors exhibit a Stokes shift around $\sim$50 nm. Only a small portion of the absorption and emission spectra overlap; therefore, these compounds are largely transparent to their own emitted light.

2,5-Diphenyloxazole (PPO) and p-Terphenyl (PTP) are commonly employed as primary fluors. Both are highly soluble in polystyrene and polyvinyltoluene and exhibit good resistance to radiation damage. They have fast fluorescence decay times of about 1–1.5 ns [57] and high quantum efficiencies. These combined merits make them excellent choices for use in plastic scintillators. PPO has an emission peak around 360-365 nm [58] and PTP has around 400 nm [59].

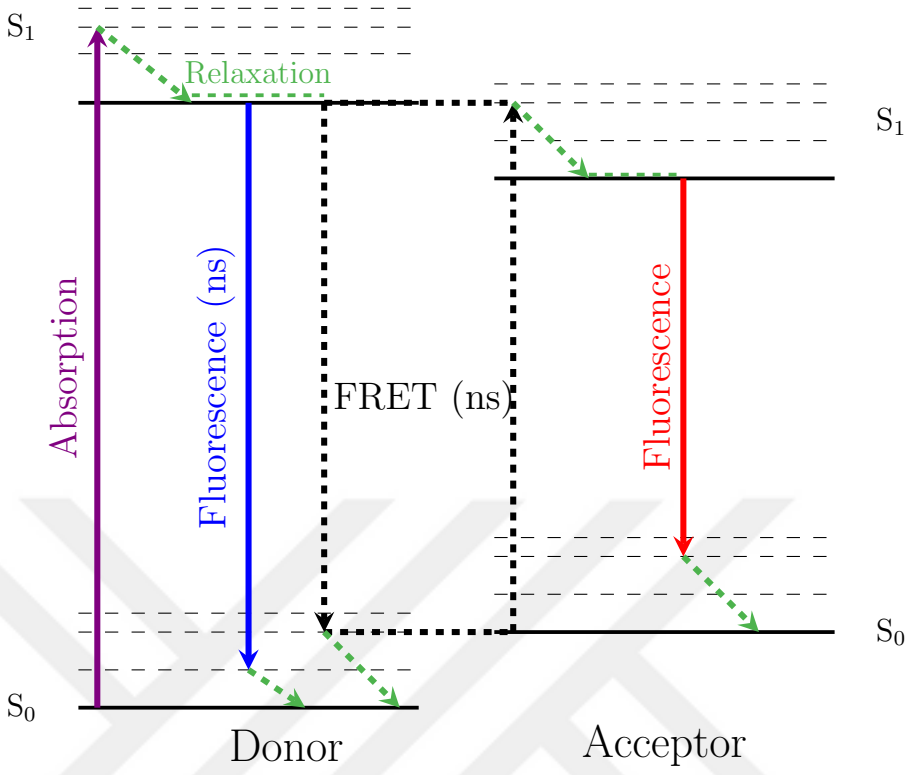

Figure 2.7. Jablonski diagram of FRET (adapted from A. M. Mooney, Wikipedia, CC BY-SA 3.0).

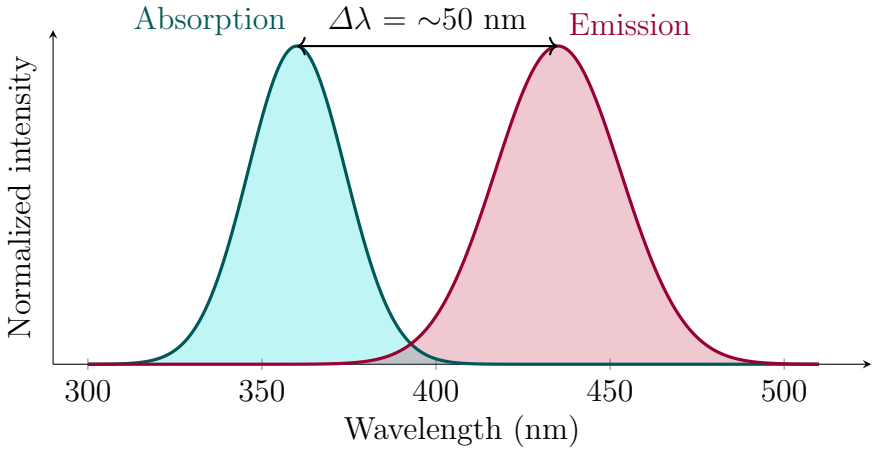

Figure 2.8. Illustration of Stokes shift of primary flours with minimal spectral overlap.

The emission spectrum of a plastic scintillator should overlap with the absorption spectrum of the light-sensitive detector it is coupled to. Fine-tuning of the scintillator's emission characteristics is achieved by the addition of secondary fluors, commonly referred to as wavelength shifters. Wavelength shifters absorb the UV emis-

sion of the primary fluor, undergo a Stokes shift, and subsequently, after around 1.5 ns [55], emit photons in the visible range. The most widely employed chemicals as wavelength shifters are 1,4-Bis(5-phenyl-2-oxazolyl)benzene (POPOP) and 1,4-Bis(2-methylstyryl)benzene (Bis-MSB), which exhibit peak emission wavelengths of 415 nm and 420 nm, respectively [60]. These compounds improve light transmission by minimizing self-absorption.

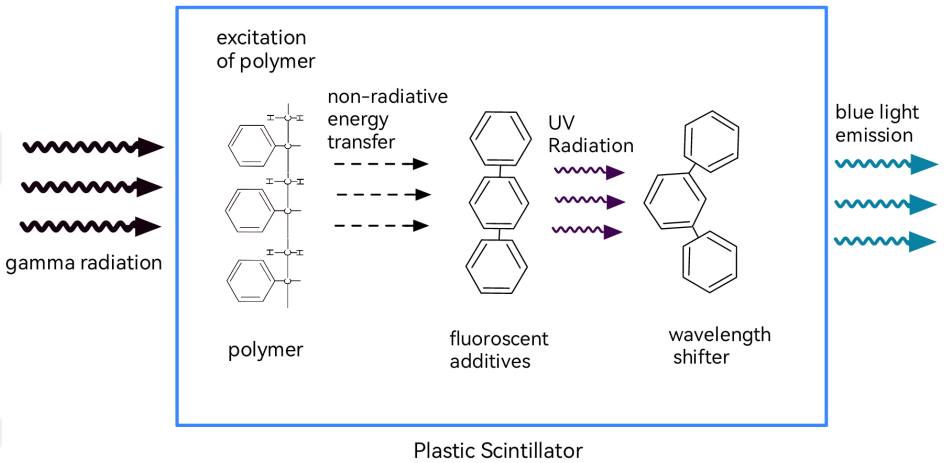

Figure 2.9. The complete scintillation process of a plastic scintillator.

Figure 2.9 illustrates the complete scintillation process in a plastic scintillator. Ionizing radiation excites the aromatic polymer matrix, which transfers its energy non-radiatively by FRET to the primary dye. The primary dye emits mainly UV photons, which are absorbed by the wavelength shifter that produces the final visible emission.

2.5.2. Characteristics

A plastic scintillator is characterized by its emission spectrum, transparency to its emission, and light output. The emission spectrum represents the wavelength distribution of photons produced during scintillation and determines the scintillator's compatibility with the light-sensitive detector. For efficient light collection, the emission spectrum should overlap with the spectral sensitivity of the PMT or SiPM. The transmission spectrum characterizes the optical transparency of the scintillator and

directly affects the efficiency of light transport to the detector. High transmittance of the visible wavelength ensures the detection of the light. The choice of polymer base, primary fluor, wavelength shifter, and their concentrations define the shape and position of the emission and transmission spectra.

The light output of a scintillator is expressed by a quantity called the light-yield, defined as the number of scintillation photons produced per unit of deposited energy, usually in photons per MeV. A higher light-yield results in a stronger signal and reduced statistical uncertainty, leading to sharper peaks and edges in the measured spectrum. This improved resolution allows better distinction between signals with small energy differences and enables the detection of lower-energy radiation. Overall, a high light-yield enhances both the sensitivity and precision of scintillation measurements.

Organic scintillators have a light-yield on the order of 10,000 photons/MeV, whereas inorganic scintillators can have light-yields up to 100,000 photons/MeV [55]. The difference between organic and inorganic scintillators arises from their emission mechanisms. In organic materials, scintillation results from molecular de-excitation within π-electron systems, which have low radiative efficiency. Inorganic crystals, on the other hand, produce light through activator luminescence involving crystal lattice defects, enabling much higher photon yields.

In practice, light-yield can be characterized either absolutely or relatively. Absolute light-yield measurements require a calibrated setup, typically involving a photodetector with known quantum efficiency and a defined optical coupling geometry. Because such measurements are sensitive to geometry and losses, they are rarely used in comparative material studies. Instead, relative light-yield measurements, performed by normalizing the light output of a sample to that of a reference material under identical conditions, are widely adopted.

3. METHODS

This thesis presents two different studies. The first study [19] investigates the effects of fluor composition and concentration on plastic scintillator characteristics. The second study [61] focuses on the effects of polymerization initiators on plastic scintillator light output.

This chapter introduces the general structure of the synthesis procedure, the experimental setup for light-yield measurements, and the data acquisition process. Chapter 4 presents effects of fluor composition and concentration on plastic scintillator characteristics, whereas Chapter 5 covers effects of polymerization initiators on plastic scintillator light output. All chemicals mentioned in the following three chapters were obtained from Sigma-Aldrich.

3.1. Synthesis

The synthesis procedure of the ternary plastic scintillator samples was carried out by thermal polymerization, which uses heat as the polymerization agent. In the process of determining optimal concentrations and the correct synthesis procedure, many samples were produced. Many others had structural defects which hamper the scintillation process.

Various complications can affect the synthesis procedure, making the scintillators unusable. Inadequate removal of oxygen and moisture results in air bubbles in the final product. Overheating, improper timing of the heating and cooling stages, and excessively rapid polymerization cause distortions, such as cracks, bubbles, cloudiness, loss of transparency, and discoloration. Figure 3.1 shows the defective samples produced during the trial and error stages.

Figure 3.1. Defective samples produced during trial and error stages.

The first step of the plastic scintillator synthesis was the choice of matrix base, primary, and secondary fluors. Then the mass calculations followed with the desired concentrations. After that, the selected monomer, which is in liquid form, was purified with activated alumina sorbent to remove inhibitors and water, as shown in Figure 3.2a.

The additives were poured into the volume of purified monomer and stirred thoroughly using a magnetic stirrer. The mixture was maintained at 40 °C and stirred for six hours to ensure homogeneous dissolution of all components. The stirring setup is shown in Figure 3.2b. High-purity Argon gas was then introduced to the homogeneous solution for two minutes to remove dissolved oxygen.

The mixture was poured into glass tubes and sealed under an argon atmosphere. The sealed tubes were kept at 100–120 °C for five days to allow polymerization to proceed. Afterwards, the samples were gradually cooled to room temperature over an additional five-day period to ensure uniform polymerization. The samples had cylindrical shapes since the glass tubes were cylindrical. This form of the samples was processed into the desired shapes and dimensions.

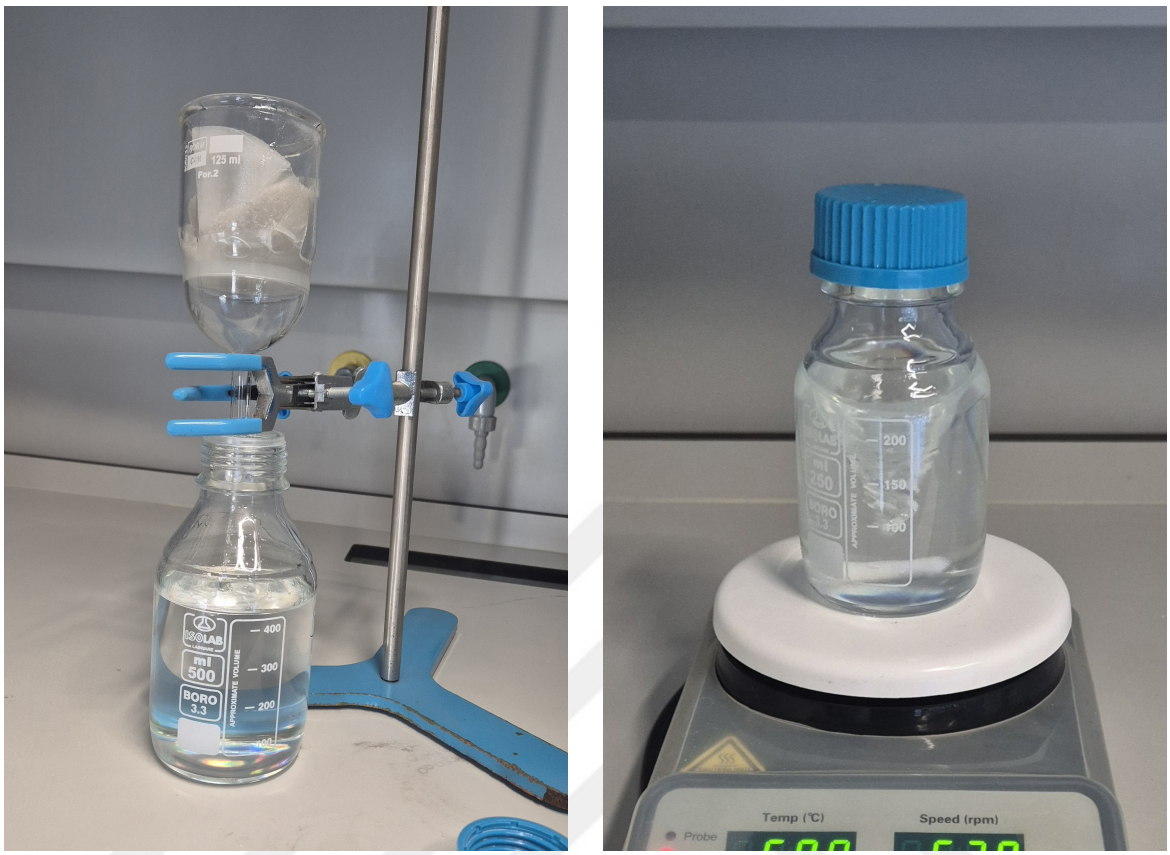

(a) (b)

Figure 3.2. (a) Purification process of the selected monomer. (b) The stirring process of the additives and the monomer.

The shaping and polishing procedures were carried out with sandpapers ranging from 400 to 4000 grit using a high-speed rotating polishing machine (ATM Saphir 150 M1, produced by QATM, Mammelzen, Germany). To obtain a symmetrical shape, polishing was carried out slowly and patiently. The samples were handled gently, without applying pressure; only their own weight should create a force on the rotating sandpaper. After each equal interval, the samples were rotated by ninety degrees around their center. Water was continuously applied to the polishing surface to prevent overheating and ensure a smooth optical finish. Figure 3.3a shows the polishing procedure.

The first useful samples were shaped into cylinders of varying dimensions and tested by coupling to appropriate PMTs. The initial measurements confirmed the

scintillation response of the synthesized materials. Figure 3.3b shows the samples produced in various sizes.

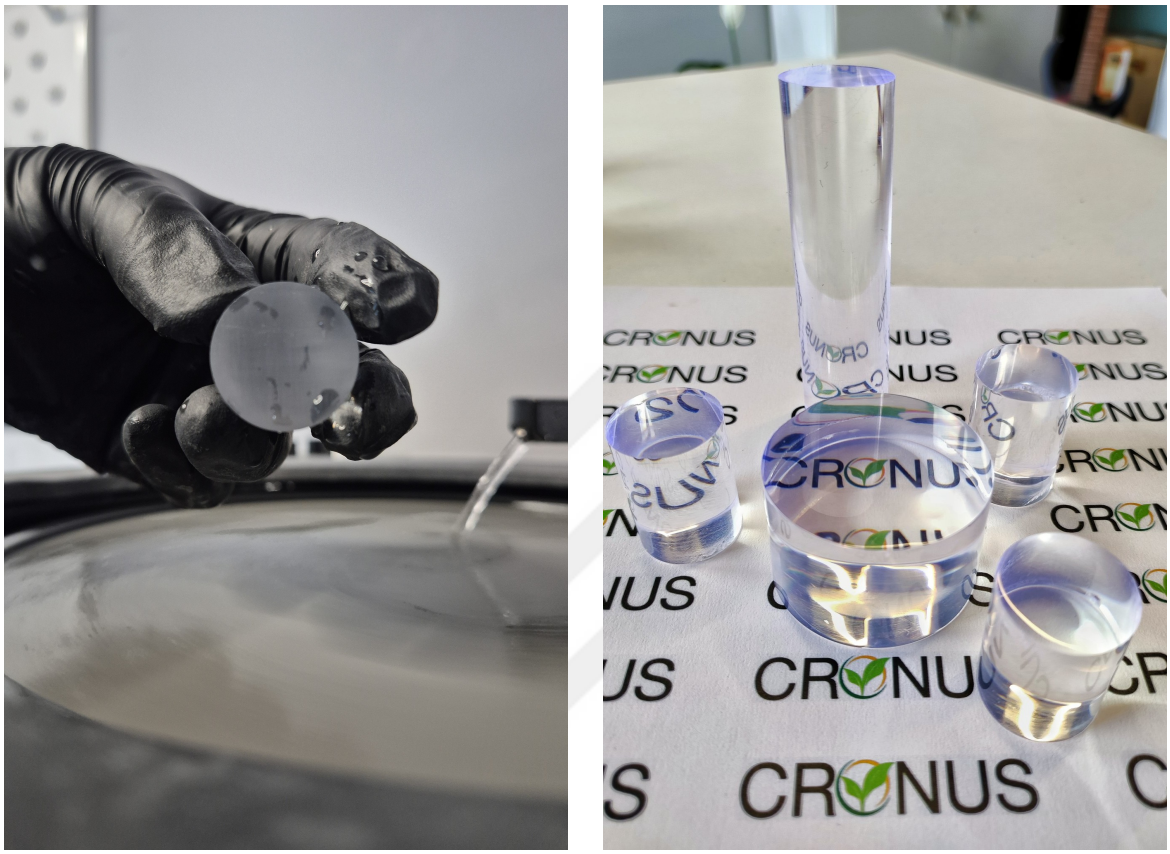

(a) (b)

Figure 3.3. (a) Polishing procedure of a plastic scintillator sample. (b) Synthesized plastic scintillator samples in various dimensions.

3.2. Experimental Setup

light-yield measurements of the two studies presented in this thesis were performed using similar but different setups; the samples were wrapped with Teflon tape and black tape to maximize reflection. Then they were coupled to a SiPM or a PMT, by Eljen EJ-550 optical silicon grease (produced by Eljen Technology, Sweetwater (TX), USA). The optical silicon grease has a refractive index of 1.46, and its transmission

is about 99% for a thickness of 0.1 mm for 430 nm and higher [62]. The scintillator detector system was placed in a wooden box with a wall thickness of 2 cm. The analog signal generated by the detector was digitized using either an oscilloscope or a dedicated digital acquisition system. The collected data were subsequently analyzed to characterize the light output of the samples.

An example setup is shown in Figure 3.4, box was covered with black sheets to reduce any light interference. The radioactive source was positioned out of the box and shielded with lead bricks for radiation protection. A Geiger counter was always present to monitor radiation levels.

Figure 3.4. An experimental setup used for light-yield measurements.

3.3. Methodology for Relative Light Yield Calculation

As mentioned in Section 2.5.2, absolute light yield measurement requires a calibrated setup, and its necessity is often outweighed by the complexity of the procedure. Studies presented in this thesis adopt a relative light yield measurement method for light output characterization. This method utilizes a reference sample, preferably one with a known absolute light yield value, alongside the synthesized samples. To ensure

a valid comparison, all samples were investigated under the exact same experimental conditions.

The samples were characterized by their gamma-ray spectra. When a scintillator interacts with gamma-rays, the resulting pulse height spectrum, which is a plot of the recorded energy versus the number of detected events (counts), reveals distinct features that characterize the scintillation material and the incident gamma-rays. This spectrum is generally divided into two main components: the photopeak and the Compton continuum.

The photopeak corresponds to the events where the incident gamma-ray deposits all of its energy within the scintillator. This occurs primarily through the photoelectric effect and the absorption of any secondary radiation. The photopeak appears as a distinct, Gaussian-shaped peak at the pulse amplitudes corresponding to the full energy of the incident gamma-rays.

The Compton continuum is the broad part of the spectrum. It results from Compton scattering events where the incident gamma-ray interacts with an electron in the crystal but only deposits a fraction of its energy before escaping the detector; therefore, it corresponds to a lower energy region than the photopeak. This continuum extends up to a sharp boundary called the Compton edge, which represents the maximum energy transferred to an electron in a single scattering event.

The probability of the photoelectric effect depends on the effective atomic number (Z_{eff}) of the absorbing material. This dependency approximately scales with Z_{eff}^5 [63]. However, organic scintillators are composed of low-Z content; therefore, they do not show photopeaks in their gamma spectra. The standard light-yield measurement method for organic scintillators uses the Compton edge of a gamma source with a known energy spectrum.

The relative light yield of the samples was determined by comparing their Compton edge positions to that of a reference sample with a known light-yield. The method proceeds as follows: a Gaussian is fitted to the energy distribution around the Compton edge of the spectrum, then a certain fraction of the Gaussian peak corresponds to the Compton edge energy value of the scintillator. The relative light yield is calculated as

$$RLY_{sample} = RLY_{ref} \times \frac{CE_{sample}}{CE_{ref}} \tag{3.1}$$

where RLY_{sample} is the relative light yield of the synthesized sample, RLY_{ref} is the relative light yield of the reference scintillator, CE_{sample} is the extracted Compton edge position of the sample and CE_{ref} is the Compton edge position of the reference sample. RLY_{ref} is set to 100, and the relative light yields of all other samples are expressed as percentages of this value.

In the literature, the suggested position of the Compton edge energy varies between different percentages of the Gaussian peak [64]. As investigated by Safari *et al.* [65], the precise position of the Compton edge and the optimal choice of this fraction depend on the detector response and the gamma-ray energy. Therefore, fine-tuning is often a little more than an educated guess.

4. THE EFFECTS OF FLUOR COMPOSITION AND CONCENTRATION ON PLASTIC SCINTILLATOR LIGHT OUTPUT

In this study, the definitive versions of three different samples employed polyvinyltoluene as the polymer base; PPO and PTP as primary fluors; and POPOP and Bis-MSB as wavelength shifters. The first sample, labeled as CR-1, contains 1.5% PPO and 0.08% POPOP. CR-2 contains 1.5% PTP and 0.08% Bis-MSB. The last sample, CR-3, contains 0.75% PPO and 0.75% PTP as primary fluors, 0.04% POPOP and 0.04% Bis-MSB as wavelength shifters. The concentrations of the samples are presented in Table 4.1.

Table 4.1. List of scintillator samples and their incorporated additives.

Sample	**Primary fluor (wt%)**	**Wavelength shifter (wt%)**
CR-1	1.5% PPO	0.08% POPOP
CR-2	1.5% PTP	0.08% Bis-MSB
CR-3	0.75% PPO + 0.75% PTP	0.04% POPOP + 0.04% Bis-MSB

The next step was the characterization of the synthesized samples. To compare their light output, the relative light yields were measured using the Compton edge method. A commercially available scintillator from Eljen Technology (EJ-204) was used as the reference sample. It was a cube with a side length of 10 mm. Therefore, the synthesized samples were cut and polished to match the same shape and dimensions. Figure 4.1 shows the synthesized cubic samples and the reference sample.

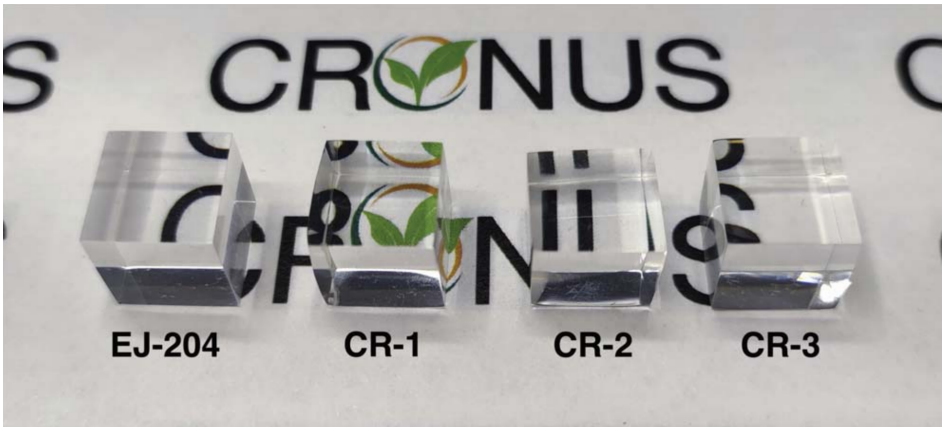

Figure 4.1. The synthesized plastic scintillator samples and the reference sample.

4.1. Experimental Setup and Data Acquisition

The samples were characterized by their light output, emission spectra, and transmission distributions. The light-yield measurements were performed using the following setup. Considering the dimensions of the plastic scintillator samples, an Onsemi J-series SiPM with the size of 6 × 6 mm (MICROFJ-60035-TSV) was used as a photodetector, and 10 × 10 mm plastic scintillator samples were coupled with it using Eljen EJ-550 optical silicon grease. A low-voltage power supply was connected to the SiPM biasing board. The output signal was amplified via a CAEN N978 fast amplifier, and the signal shape is digitized and recorded by a Keysight MXR254A oscilloscope.

^{137}Cs was selected as the radioactive source since it has a clear Compton-edge at 477.3 keV. The plastic scintillators were wrapped with aluminum foil and plastic tape and located inside a wooden box with a wall thickness of 2 cm. The ^{137}Cs source was positioned 20 cm away from the scintillator.

For each scintillator samples 10^5 data sets were taken and averaged. The signal shapes for the prepared scintillator samples and EJ-204 are shown in Figure 4.3a. Peak normalization is applied to the signal shape distributions. Since the fluors in the plastic scintillator samples have different timing properties, the signal width of the scintillator

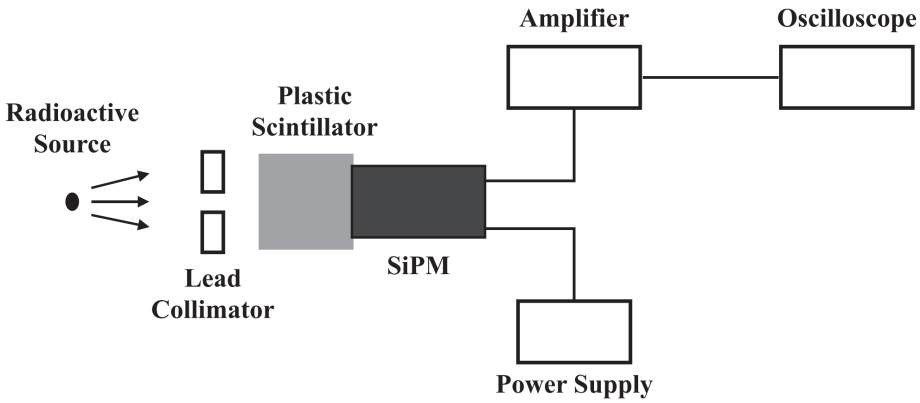

Figure 4.2. A schematic view of the experimental setup for light-yield measurement.

samples is not identical. Therefore, energy deposition estimation was performed by measuring the area under the pulse shapes instead of by measuring pulse height.

4.2. Analysis

Since organic scintillators don't show photo-peaks due to their low-Z content, the determination of light-yield was performed by measuring the Compton-edge location. For this purpose, the edge region in the energy distribution was fitted with a Gaussian function, the height of the Gaussian peak was determined, and the edge location was taken to be the energy corresponding to a certain percentage of the peak height [64]. The suggested values in the literature vary from 66% to 89%, but the optimum value changes depending on the detector and scintillator. Since choosing a specific percentage of the local Compton maximum is not an ideal way to represent the Compton-edge location [65], the percentage values were chosen from 90% to 50% in 10% steps to determine the relative light output. We consider that evaluating the relative light yield output with different percentage values is a more conservative approach than what is suggested in the literature.

The fit ranges of the Gaussian function of each distribution were chosen in such a way that once the fit is performed and has successfully converged, the peak value of the distribution stays within the fit range, and the lower end of the range was at least half a sigma away from the peak. We also note that changing these lower ends

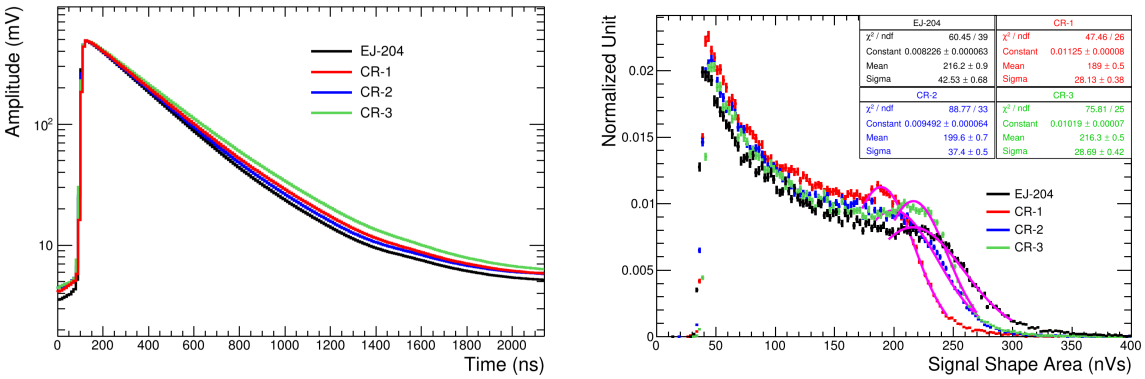

(a) (b)

Figure 4.3. (a) Signal shapes of EJ-204 and the produced plastic scintillator samples. (b) Signal shape areas and fit parameters.

by ± 10 nVs affected the relative light yields by less than 1% for all of the fits. The Gaussian fits are shown in Figure 4.3b.

The relative light yields of the prepared plastic scintillator samples were determined from the EJ-204 commercial scintillator sample produced by Eljen Technology by

$$RLY_{sample} = RLY_{EJ-204} \times \frac{A_{CE,sample}}{A_{CE,EJ-204}} \tag{4.1}$$

where RLY is the relative light yield and A is the signal shape area of the selected Compton-edge position. Since the light-yield information of EJ-204 is already given by Eljen Technology as 10 400 ph/MeV, the relative light yield of EJ-204 was taken as 100 at each selected percentage value, and the relative light yield of the prepared plastic scintillator samples was calculated based on it.

4.3. Results

The obtained relative light yield values at each selected percentage value are listed in Table 4.2. The measurements showed that the maximum deviations from the relative light yield at 90% to 50% are 2.7% for CR-1, 0.4% for CR-2, and 3.3% for CR-3. The

LYs were estimated by taking EJ-204 as a reference and found to be 8788 ± 42 for CR-1, 9537 ± 10 for CR-2, and 9932 ± 52 for CR-3. The results indicate that CR-3 (0.75% PPO + 0.75% PTP and 0.04% POPOP + 0.04% Bis-MSB) has the highest LY value among the produced samples.

Table 4.2. The RLY and LY values of the produced plastic scintillator samples with respect to EJ-204 with mean squared error estimation.

Sample name	**RLY (%)**					**Average RLY**	**LY (photons/MeV)**
	90	**80**	**70**	**60**	**50**		
EJ-204	100	100	100	100	100	100	10 400
CR-1	85.7	85.0	84.5	83.9	83.4	84.5 ± 0.4	$8\,788 \pm 42$
CR-2	91.9	91.8	91.6	91.5	91.5	91.7 ± 0.1	$9\,537 \pm 10$
CR-3	97.3	96.2	95.3	94.6	94.0	95.5 ± 0.5	$9\,932 \pm 52$

The optical properties of the synthesized plastic scintillator samples in the visible light wavelength range are investigated using a Jasco V-730 UV-Vis spectrophotometer and compared with an EJ-204 plastic scintillator reference sample of the same geometrical shape. The transmission factors as a function of light wavelength are presented in Figure 4.4. The transmission factors of all the produced samples are comparable with EJ-204 and surpass 86% after 440 nm.

In addition, the emission wavelength distribution of the produced plastic scintillator samples and the EJ-204 sample is shown in Figure 4.5. The emission wavelength distributions are measured using a Jasco FP-8300 Spectrofluorometer by scanning excitation wavelengths from 200 nm to 400 nm. Since the samples consist of different types of primary and secondary fluor, the peak of the emission wavelengths shows up at different values: 410 nm for EJ-204, 423 nm for CR-1, 431 nm for CR-2, and 428 nm for CR-3. The PDE curve of the Onsemi J-Series SiPM, which peaks at 430-440 nm, is also presented in the emission distribution [66]. The PDE of the scintillator samples at the emission peak values differ by about 1%. The emission peak of each scintillator lies within the wavelength range where the SiPM exhibits its highest photon detection efficiency.

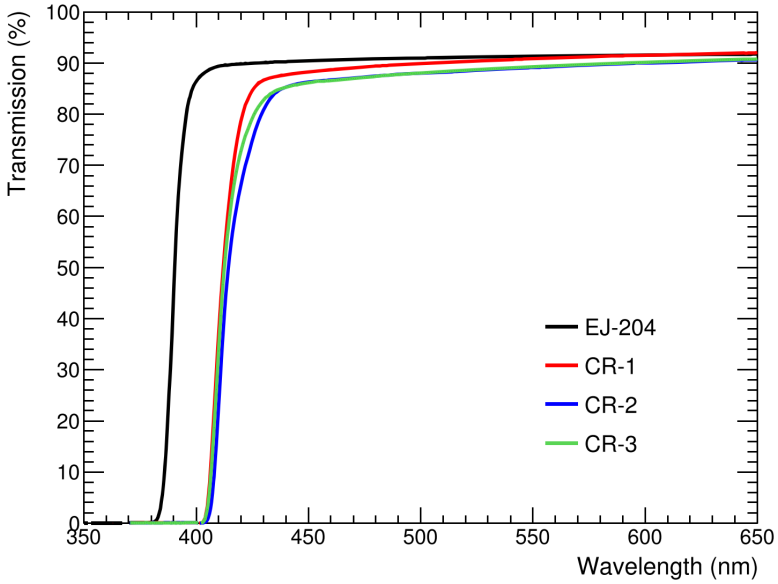

Figure 4.4. Transmission distributions of EJ-204 and the produced plastic scintillator samples.

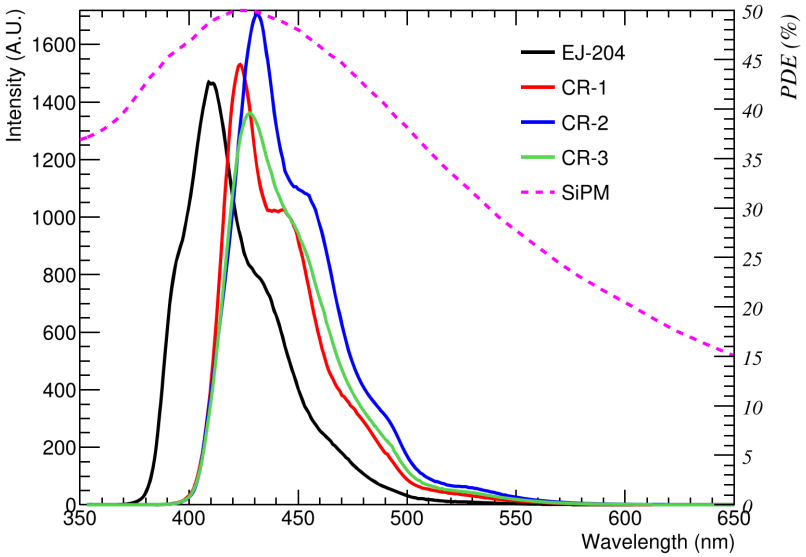

Figure 4.5. Emission distributions of EJ-204 and the produced plastic scintillator samples and PDE curve of Onsemi J-series SiPM [66].

5. THE EFFECTS OF POLYMERIZATION INITIATORS ON PLASTIC SCINTILLATOR LIGHT OUTPUT

The second study focused on the effects of polymerization initiators on the light output of plastic scintillators. In order to enhance the performance of the produced plastic scintillator samples, it is critical to optimize the synthesis procedure. To regulate the polymerization procedure, various chemicals are employed as initiators [67]. A polymerization initiator generates radicals when exposed to heat, which links monomers to form polymers. Polymerization initiators lower the processing temperature, enhance reaction consistency, and shorten the process time. However, initiators may diminish the performance of the final product; therefore, determining their optimal amounts is critical.

The two polymerization initiators most frequently reported [68–72] in plastic scintillator synthesis, 2,2-Azobis(2-methylpropionitrile) (AIBN, CAS No: 78-67-1) and benzoyl peroxide (BPO, CAS No: 94-36-0), were selected for this study. In the literature, the concentrations of initiator loadings vary in the range 0.01–1.0 wt% [71–75], without a suggested concentration. To resolve any influence on light-yield, three representative concentrations, 0.2, 0.5, and 1.0 wt%, were examined.

As the study focused on the effects of initiators, all synthesized samples had the same matrix base, primary, and secondary fluors at the same weight percentages. polystyrene was used as the polymer matrix due to its compatibility with the chosen initiators [76, 77]. PPO was chosen as the primary fluor (1.5 wt%) and POPOP was chosen as the wavelength shifter (0.08 wt%).

The synthesis procedure followed the same steps as the previous one. However, in this case, the heating cycle lasted 10 days which followed by a 5-day cooling cycle. Also, the scintillators were shaped into cylindrical tubes with a diameter of 25 mm and a length of 15 mm.

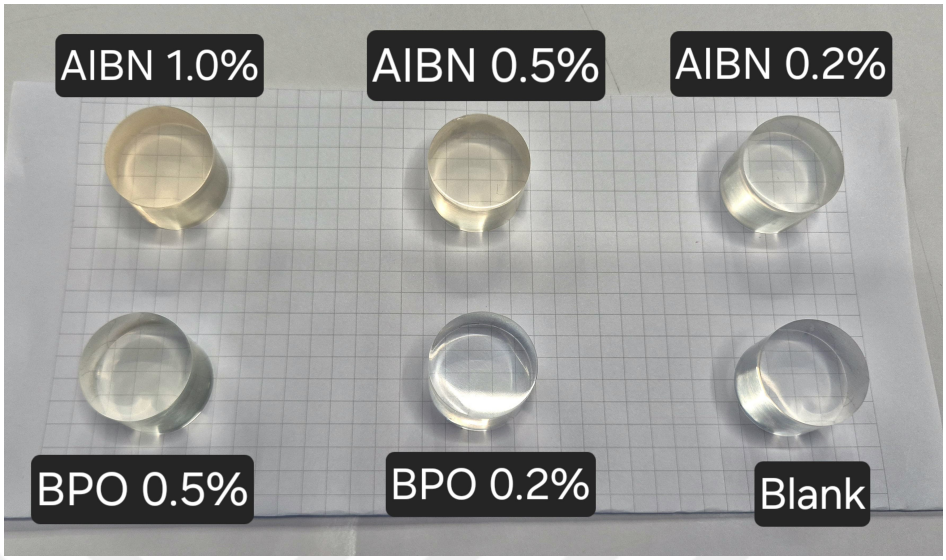

Figure 5.1. The synthesized initiator-loaded plastic scintillator samples and the reference sample.

Five plastic scintillator samples were produced with different molar percentages of polymerization initiators, along with a reference sample. Three different molar percentages were examined for AIBN (0.2%, 0.5%, and 1.0%) and two for BPO (0.2% and 0.5%). Figure 5.1 shows the synthesized plastic scintillator samples labeled as Blank, AIBN 0.2%, AIBN 0.5%, AIBN 1.0%, BPO 0.2%, and BPO 0.5%. The labels indicate the type and molar percentage of the initiator used in each sample.

5.1. Experimental Setup and Data Acquisition

Figure 5.2 shows the schematic diagram of the experimental setup. The samples were coupled to a Hamamatsu R7525HA-2 PMT (produced by Hamamatsu Photonics, Hamamatsu City, Japan) using Eljen EJ-550 optical silicon grease and wrapped in aluminum to enhance reflection. The PMT–plastic scintillator system was placed in a wooden box with a wall thickness of 2 cm. The PMT was connected to a CAEN DT5790 [78] digital acquisition system, which was operated at 1300 V. Each scintillator sample was measured under identical digitizer settings until 1.5×10^5 valid events were recorded. The CAEN DT5790 operates at a 250 MS/s sample rate with 12-bit resolution settings.

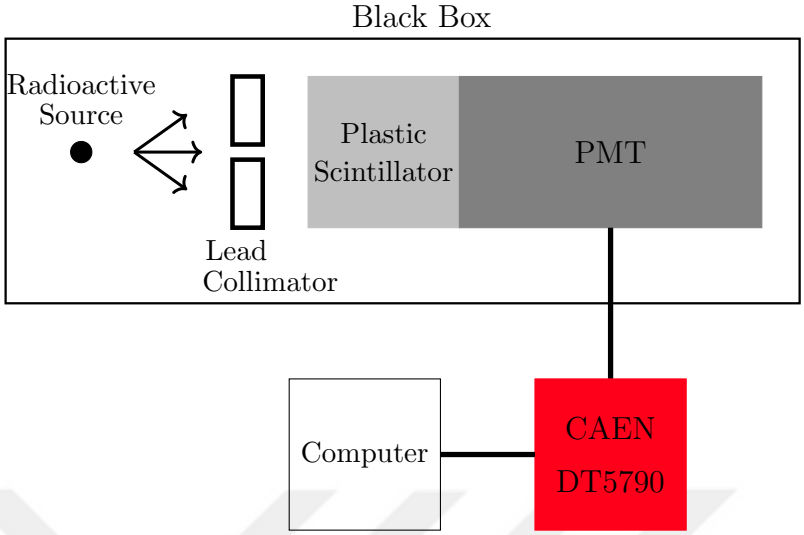

Figure 5.2. Schematic diagram of the experimental setup used in study II.

Light output characterization was carried out at different gamma energy values. The four different gamma sources used in this study are presented in Table 5.1. ^{22}Na exhibits two different gamma lines of energies 511 keV and 1275 keV, with corresponding Compton edge energies of 341 keV and 1062 keV. ^{137}Cs produces a gamma-ray of 662 keV energy with a Compton energy of 478 keV. ^{54}Mn emits a gamma-ray of energy 835 keV, with a corresponding 640 keV of Compton edge energy. ^{60}Co produces two gamma-rays with energies 1173 and 1333 keV. Since the energy values differ only by 155 keV, they cannot be resolved by our detector. The measured spectrum, therefore, represents the sum of the responses to both gamma lines. The effective Compton edge energy of ^{60}Co is obtained, intensity-weighted, as 1041 keV.

5.2. Analysis

The energy distributions around the Compton edge were fitted with Gaussian functions. The study presented in Chapter 4, from Akgün *et al.* [19], evaluated Compton edge values at 50%, 60%, 70%, 80%, and 90% of the Gaussian peak, and the 80% measurement most accurately reflected the average values, as shown in Table 4.2.

Table 5.1. Radioactive sources used in this study and their gamma-ray and Compton edge energies.

Radioactive source	**Gamma-ray energy (keV)**	**Compton edge energy (keV)**
^{22}Na	511, 1275	341, 1062
^{137}Cs	662	478
^{54}Mn	835	640
^{60}Co	1174, 1333	1041

In this study, RLY is measured at 50%, 60%, 70%, 80%, and 90%; however, to ensure consistency, the results present the evaluations at 80%. The fit ranges of the Gaussian function were chosen so that the peak value of the measurement stays within the range and a ±5 unit shift in both ends results in only a 0.6% difference in the mean RLY values. A detailed description of the Gaussian fit process is presented in Appendix A. The RLY of the prepared plastic scintillator samples is calculated by the described method with the following formula,

$$RLY_{sample} = RLY_{Blank} \times \frac{CE_{sample}}{CE_{Blank}} \tag{5.1}$$

where CE_{sample} and CE_{Blank} are calculated Compton edge values at 80% of the Gaussian peak, RLY_{Blank} is taken as 100, and the RLY of the prepared plastic scintillator samples was calculated based on it.

5.3. Results

Figure 5.3 shows the energy distributions and Gaussian fits. The navy blue graph is for the source ^{22}Na. ^{22}Na decays by emitting two different gamma-rays; therefore it exhibits two different Compton edges. The first one is at 341 keV and the second is at 1062 keV. The green graph is for ^{137}Cs with a Compton edge at 478 keV. The purple graph is ^{54}Mn with a Compton edge at 640 keV. The black graph is for ^{60}Co with a Compton edge at 1041 keV. Comparisons among Blank, AIBN 0.2%, AIBN 0.5%, and AIBN 1.0%, and among Blank, BPO 0.2%, and BPO 0.5% show that as the initiator content increases, the energy graphs exhibit narrower peaks, implying lower energy resolution and low light output.

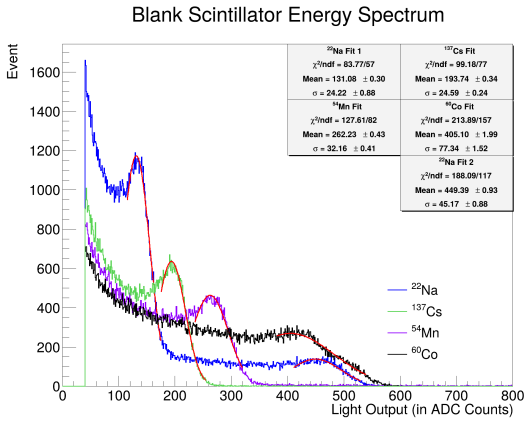

(a) Blank

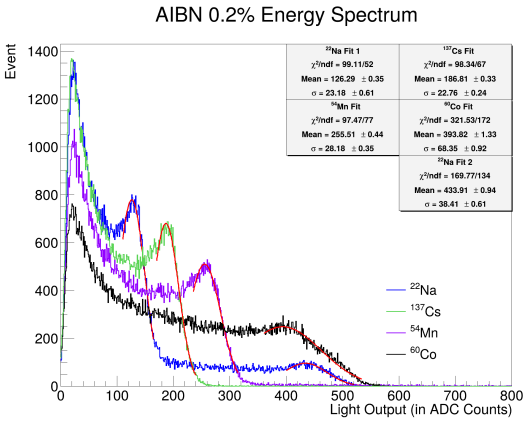

(b) AIBN 0.2%

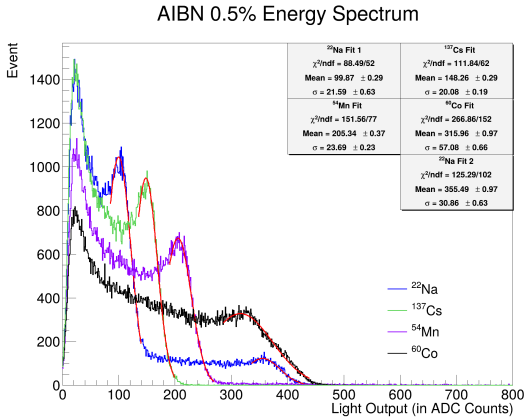

(c) AIBN 0.5%

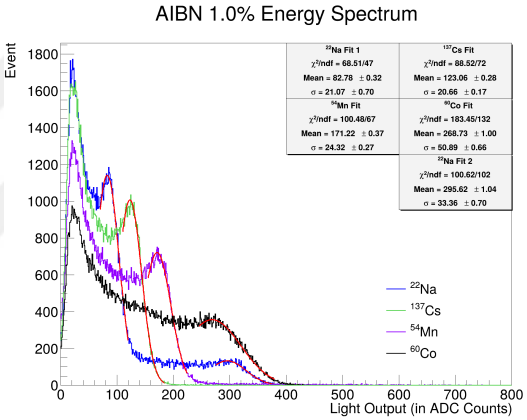

(d) AIBN 1.0%

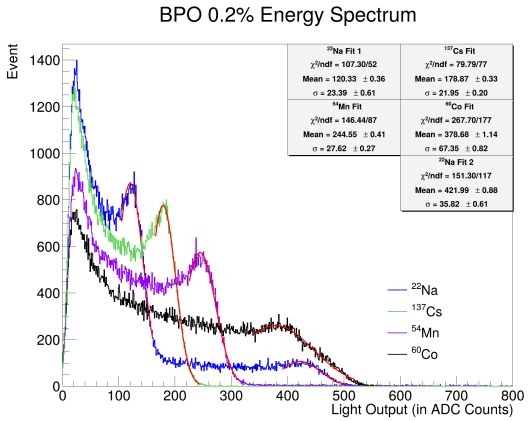

(e) BPO 0.2%

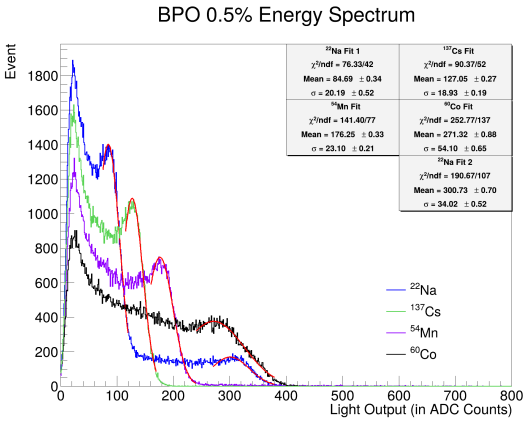

(f) BPO 0.5%

Figure 5.3. Energy distributions of the prepared samples with applied Gaussian fits (red lines): (a) Blank, (b) AIBN 0.2%, (c) AIBN 0.5%, (d) AIBN 1.0%, (e) BPO 0.2%, and (f) BPO 0.5%.

Table 5.2. Point-by-point relative light yield values, in %, at each Compton edge energy. All values are given with respect to the blank scintillator.

Scintillator	^{22}Na @ 341 keV (%)	^{137}Cs @ 478 keV (%)	^{54}Mn @ 640 keV (%)	^{60}Co @ 1041 keV (%)	^{22}Na @ 1062 keV (%)
Blank	100.0 ± 0.0	100.0 ± 0.0	100.0 ± 0.0	100.0 ± 0.0	100.0 ± 0.0
AIBN 0.2%	96.1 ± 0.5	96.2 ± 0.6	96.8 ± 0.4	96.2 ± 0.2	95.8 ± 0.1
AIBN 0.5%	77.5 ± 0.4	76.9 ± 0.5	78.0 ± 0.3	77.5 ± 0.3	78.5 ± 0.2
AIBN 1.0%	65.9 ± 0.5	65.2 ± 0.3	66.2 ± 0.3	66.2 ± 0.3	66.3 ± 0.3
BPO 0.2%	92.4 ± 0.6	92.2 ± 0.3	92.7 ± 0.3	92.7 ± 0.1	92.9 ± 0.2
BPO 0.5%	66.5 ± 0.3	66.6 ± 0.5	67.6 ± 0.3	67.3 ± 0.2	67.5 ± 0.4

The obtained RLY values for each energy value are listed in Table 5.2. AIBN 0.2% exhibits an RLY of 96.1% at the 341 keV Compton edge of ^{22}Na, 96.2% at the 478 keV Compton edge of ^{137}Cs, 96.8% at the 640 keV Compton edge of ^{54}Mn, 96.2% at the 1041 keV Compton edge of ^{60}Co, and 95.8% at the 1062 keV Compton edge of ^{22}Na. Across these energy values, the RLY remains steady, with only a 1.0% variation.

AIBN 0.5% has a minimum RLY of 77.5% at 341 keV and a maximum RLY of 78.5% at 1062 keV, while AIBN 1.0% shows a minimum RLY of 65.2% at 478 keV and a maximum RLY of 66.3% at 1062 keV. BPO 0.2% has a minimum RLY of 92.2% at 478 keV and a maximum RLY of 92.9% at 1062 keV, whereas BPO 0.5% exhibits a minimum RLY of 66.5% at 341 keV and a maximum RLY of 67.6% at 640 keV. The largest difference in RLY for a sample is 1.1%. Overall, the light outputs of the scintillators remain consistent across different energy values, and for each Compton edge, the RLY decreases as the initiator concentration increases.

Table 5.3 presents the average RLY values of different energies for each scintillator, along with RMS errors; a detailed explanation of error propagation is given in Appendix B. AIBN 0.2% exhibits an average RLY of (96.2 ± 0.3)%, AIBN 0.5% exhibits an average RLY of (77.7 ± 0.5)%, and AIBN 1.0% exhibits an average RLY of (66.0 ± 0.4)%. While the decrease in light output for AIBN 0.2% is relatively small (3.8%), AIBN 0.5% shows a decrease of 22.3%, and AIBN 1.0% exhibits a decrease

Table 5.3. Average relative light yield values and associated errors, all measured relative to the blank scintillator.

Scintillator	**Mean RLY (%)**	**RLY error (%)**
Blank	100.00	0.0
AIBN 0.2%	96.2	0.4
AIBN 0.5%	77.7	0.5
AIBN 1.0%	66.0	0.4
BPO 0.2%	92.6	0.3
BPO 0.5%	67.1	0.5

of 34.0%. Losing one-third of the attainable light would cause a notable decrease in resolution.

BPO 0.2% exhibits an average RLY of (92.6 ± 0.2)% and BPO 0.5% exhibits an average RLY of (67.1 ± 0.4)%. In this case, the use of 0.2% initiator results in a 7.4% decrease in light output, which is greater than the loss observed for AIBN at 0.2%. At 0.5%, the loss in light output is 32.9%, comparable to the loss observed in the 1.0% case of AIBN. Figure 5.4 illustrates the results in Table 5.3 and depicts the trend of decrease in mean RLY with increasing initiator concentration.

A reliable scintillator should exhibit a linear relation between the deposited energy and the light output. The linearity ensures that as energy changes, the response of the scintillator remains the same; therefore, the scintillator can be employed and trusted to compare different energy values.

In Figure 5.5, each sample is plotted with a different marker shape, illustrating the near-linear relationship between Compton edge energy and measured light output. Notably, the Blank Scintillator (black circles) maintains the highest response at each energy, indicating superior LY relative to doped samples. These findings confirm that, while the detector response remains linear with energy, chemical doping can measurably diminish scintillation performance.

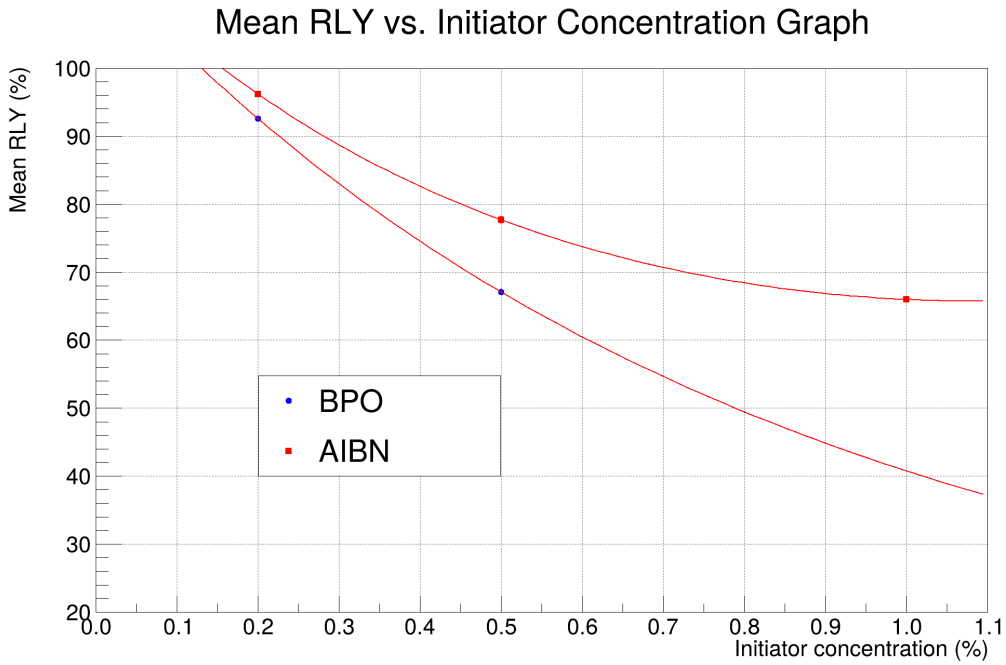

Figure 5.4. Illustration of the results in Table 5.3.

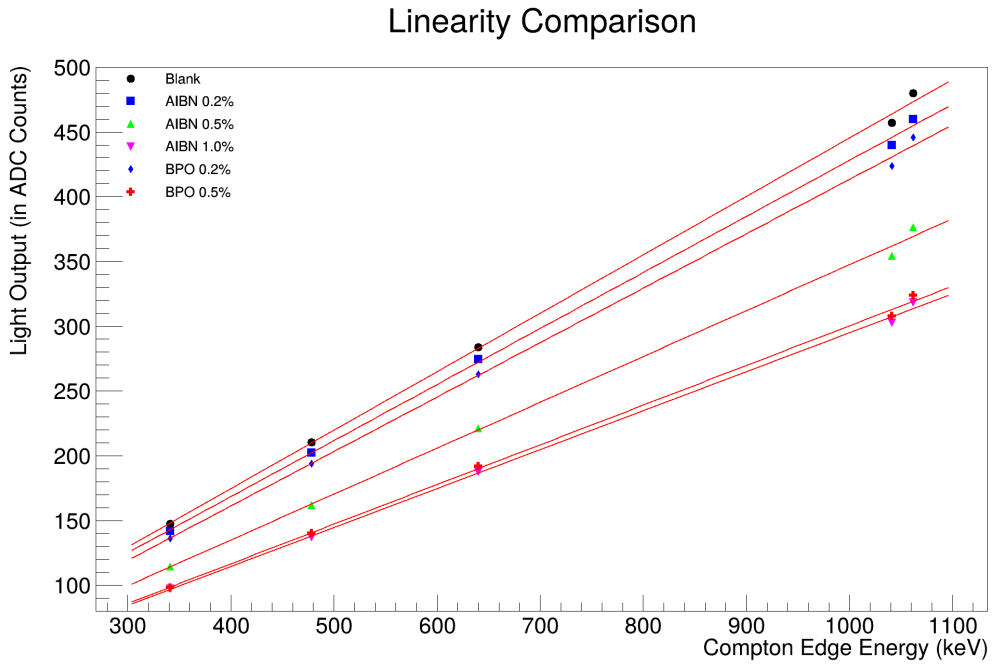

Figure 5.5. Response of the scintillator samples. Red lines indicate the linear fits for each sample.

6. CONCLUSION

The detection of ionizing radiation plays an essential role in modern science and technology. Many fields, including medical imaging, high-energy physics, nuclear power, and security, rely on reliable radiation detectors. Among the available techniques, plastic scintillator systems offer a cost-effective, robust, long-lived, and application-specific solution. The studies presented in this thesis investigated the optimization of plastic scintillator synthesis.

In the first study, three different plastic scintillator samples are synthesized, all of which employ polyvinyltolueneas a polymer base. CR-1 includes 1.5% PPO and 0.08% POPOP, CR-2 includes 1.5% PTP and 0.08% Bis-MSB, CR-3 includes (0.75%PPO + 0.75%PTP) as primary fluors and (0.04% POPOP + 0.04% Bis-MSB) as wavelength shifters. All three samples are synthesized under the exact same conditions. Their optical characteristics are compared to a commercial scintillator produced by Eljen Technology, EJ-204.

The transmission factors of all the produced samples are comparable with EJ-204 and surpass 86% after 440 nm. The peak of emission wavelengths are 423 nm for CR-1, 431 nm for CR-2, and 428 nm for CR-3. The PDE of the scintillator samples at the emission peak values differ by about 1% when used with a Onsemi J-series SiPM. The measurements show that the maximum deviations from the relative LY at 90% to 50% are 2.7% for CR-1, 0.4% for CR-2, and 3.3% for CR-3. The light-yields are estimated by taking EJ-204 as a reference and found to be 8788 $\pm$ 42 for CR-1, 9537 $\pm$ 10 for CR-2, and 9932 $\pm$ 52 for CR-3. The results indicate that CR-3 (0.75% PPO + 0.75%PTP and 0.04% POPOP + 0.04% Bis-MSB) has the highest light-yield value among the produced samples.

The second study investigated the effects of polymerization initiators. AIBN and BPO are selected as polymerization initiators. To investigate their effects on the

light output of plastic scintillators, six samples with the same constituents and concentrations are synthesized. All samples employ polystyrene as polymer base, contain 1.5% PPO and 0.08% POPOP. One of the samples does not contain any polymerization initiator and is set as the reference sample; it is named Blank.

AIBN is investigated at three different molar percentage values: 0.2%, 0.5%, and 1.0%. Samples are named as AIBN 0.2%, AIBN 0.5%, and AIBN 1.0%, respectively. BPO is investigated for two different molar percentage values: 0.2% and 0.5%. The samples are named as BPO 0.2% and BPO 0.5%, respectively. RLY of these samples are measured as percentages of Blank. AIBN 0.2% has (96.2±0.4)%; AIBN 0.5% has (77.7±0.5)%; AIBN 1.0% has (66.0±0.4)% mean RLY. BPO 0.2% has (92.6±0.3)% mean RLY, BPO 0.5% exhibits (67.1±0.5)% RLY. Light output of doping 0.5% BPO is comparable to the 1.0% case of AIBN. 0.2% doping of selected initiators effects the light output by 3.8%-7.4%, and provides a lower processing temperature, reaction consistency, and shorten the process time. However, doping 1.0% AIBN or 0.5% BPO costs a third of the light output, which is a significant reduction.

The samples are also tested at different energy values. Light output of a scintillator should be proportional at different energy values, that means as the energy of the incoming radiation increases, the light output of the scintillator also increase linearly. This examination revealed that despite light output reductions, the detectors maintained a linear response with energy, indicating that polymerization initiator doping does not compromise the basic detection principle.

Polymerization initiators can thus be effectively employed in plastic scintillator production, provided their concentrations remain within acceptable bounds for detector systems in diverse applications, including medical imaging, nuclear reactor monitoring, high-energy physics experiments, and security checkpoint devices. Maintaining initiator concentrations around 0.2% ensures optimal optical performance while benefiting from improved manufacturing efficiency.

REFERENCES

1. Beaulieu, L. and S. Beddar, "Review of Plastic and Liquid Scintillation Dosimetry for Photon, Electron, and Proton Therapy", *Physics in Medicine & Biology*, Vol. 61, No. 20, p. R305, 2016.

2. Beddar, A. S., "Plastic Scintillation Dosimetry and Its Application to Radiotherapy", *Radiation Measurements*, Vol. 41, pp. S124–S133, 2006.

3. Ozturk, S., "Nuclear Reactor Monitoring with Gadolinium-Loaded Plastic Scintillator Modules", *Nuclear Instruments and Methods in Physics Research Section A: Accelerators, Spectrometers, Detectors and Associated Equipment*, Vol. 955, p. 163314, 2020.

4. Aad, G., T. Abajyan, B. Abbott, J. Abdallah, S. A. Khalek, A. A. Abdelalim, R. Aben, B. Abi, M. Abolins, O. S. AbouZeid and The ATLAS Collaboration, "Observation of a New Particle in the Search for the Standard Model Higgs Boson with the ATLAS Detector at the LHC", *Physics Letters B*, Vol. 716, No. 1, pp. 1–29, 2012.

5. Arnison, G., A. Astbury, B. Aubert, C. Bacci, G. Bauer, A. Bézaguet, R. Böck, T. Bowcock, M. Calvetti and The UA1 Collaboration, "Experimental Observation of Isolated Large Transverse Energy Electrons with Associated Missing Energy at s=540 GeV", *Physics Letters B*, Vol. 122, No. 1, pp. 103–116, 1983.

6. Armengaud, E., C. Augier, A. Benoıˆt, L. Bergé, T. Bergmann, J. Blümer, A. Broniatowski, V. Brudanin, B. Censier, M. Chapellier and The EDELWEISS Collaboration, "Background Studies for the EDELWEISS Dark Matter Experiment", *Astroparticle Physics*, Vol. 47, pp. 1–9, 2013.

7. Mei, D.-M. and A. Hime, "Muon-Induced Background Study for Underground

Laboratories", *Physical Review D*, Vol. 73, p. 053004, 2006.

8. Williamson, J. F., J. F. Dempsey, A. S. Kirov, J. I. Monroe, W. R. Binns and H. Hedtjärn, "Plastic Scintillator Response to Low-Energy Photons", *Physics in Medicine & Biology*, Vol. 44, No. 4, p. 857, 1999.

9. Lee, H. J., J. H. So, C. S. Kang, G. B. Kim, S. R. Kim, J. H. Lee, M. K. Lee, W. S. Yoon and Y. H. Kim, "Development of a Scintillation Light Detector for a Cryogenic Rare-Event-Search Experiment", *Nuclear Instruments and Methods in Physics Research Section A: Accelerators, Spectrometers, Detectors and Associated Equipment*, Vol. 784, pp. 508–512, 2015.

10. Qadr, H. M., "Comparison of Energy Resolution and Efficiency of NaI (Tl) and HPGe Detector Using Gamma-Ray Spectroscopy", *Journal of Physical Chemistry and Functional Materials*, Vol. 3, No. 1, pp. 24–27, 2020.

11. Lo Presti, D., G. V. Russo, E. Leonora, S. Aiello, N. Randazzo, V. Sipala and F. Longhitano, "Characterization Technique of Sub-Millimeter Scintillating Fibers", *2011 IEEE Nuclear Science Symposium and Medical Imaging Conference (NSS/MIC)*, pp. 2104–2108, Valencia, Spain, 2011.

12. CMS Collaboration, *The CMS Hadron Calorimeter Technical Design Report*, Tech. Rep. CERN-LHCC-97-031; CMS-TDR-2, CERN, 1997.

13. Hamamatsu Photonics, "Si APDs — Hamamatsu Photonics", `https://www.hamamatsu.com/us/en/product/optical-sensors/apd/si-apd.html`, 2025, [Accessed: 30-05-2025].

14. Hamamatsu Photonics, "Head-On Type — Hamamatsu Photonics", `https://www.hamamatsu.com/eu/en/product/optical-sensors/pmt/pmt_tube-alone/head-on-type.html`, 2025, [Accessed: 30-05-2025].

15. Mirzoyan, R., M. Laatiaoui and M. Teshima, "Very High Quantum Efficiency

PMTs with Bialkali Photo-Cathode", *Nuclear Instruments and Methods in Physics Research Section A: Accelerators, Spectrometers, Detectors and Associated Equipment*, Vol. 567, No. 1, pp. 230–232, 2006.

16. Gektin, A. and M. Korzhik, *Inorganic Scintillators for Detector Systems*, Springer, Cham, 2017.

17. Zaitseva, N., A. Glenn, L. Carman, H. P. Martinez, R. Hatarik, H. Klapper and S. Payne, "Scintillation Properties of Solution-Grown Trans-Stilbene Single Crystals", *Nuclear Instruments and Methods in Physics Research Section A: Accelerators, Spectrometers, Detectors and Associated Equipment*, Vol. 789, pp. 8–15, 2015.

18. Jana, A., S. Cho, S. A. Patil, A. Meena, Y. Jo, V. G. Sree, Y. Park, H. Kim, H. Im and R. A. Taylor, "Perovskite: Scintillators, Direct Detectors, and X-ray Imagers", *Materials Today*, Vol. 55, pp. 110–136, 2022.

19. Akgün, B., S. Öztürk, K. Nurdan, V. E. Özcan, N. G. Ünel, A. Kolbaşı, E. Elibollar, A. Ünal, M. Kandemir and Y. Şahin, "Characterization of Plastic Scintillator Samples Produced by a University-SME Collaboration", *Physica Scripta*, Vol. 99, No. 5, p. 055302, 2024.

20. Brown, J. A., T. A. Laplace, B. L. Goldblum, J. J. Manfredi, T. S. Johnson, F. Moretti and A. Venkatraman, "Absolute Light Yield of the EJ-204 Plastic Scintillator", *Nuclear Instruments and Methods in Physics Research Section A: Accelerators, Spectrometers, Detectors and Associated Equipment*, Vol. 1054, p. 168397, 2023.

21. Holl, I., E. Lorenz and G. Mageras, "A Measurement of the Light Yield of Common Inorganic Scintillators", *IEEE Transactions on Nuclear Science*, Vol. 35, No. 1, pp. 105–109, 1988.

22. Hajagos, T. J., C. Liu, N. J. Cherepy and Q. Pei, "High-Z Sensitized Plastic Scintillators: A Review", *Advanced Materials*, Vol. 30, No. 27, p. 1706956, 2018.

23. Knoll, G. F., *Radiation Detection and Measurement*, John Wiley & Sons, Hoboken, NJ, 4th edn., 2010.

24. Wille, K., *The Physics of Particle Accelerators: An Introduction*, Clarendon Press, Oxford, 1st edn., 2001.

25. Wiedemann, H., *Particle Accelerator Physics*, Graduate Texts in Physics, Springer Cham, Cham, Switzerland, 4th edn., 2015.

26. Starovoitova, V. N., L. Tchelidze and D. P. Wells, "Production of Medical Radioisotopes with Linear Accelerators", *Applied Radiation and Isotopes*, Vol. 85, pp. 39–44, 2014.

27. Bethe, H., "Zur Theorie des Durchgangs Schneller Korpuskularstrahlen Durch Materie", *Annalen der Physik*, Vol. 397, No. 3, pp. 325–400, 1930.

28. Bloch, F., "Zur Bremsung Rasch Bewegter Teilchen Beim Durchgang Durch Materie", *Annalen der Physik*, Vol. 408, No. 3, pp. 285–320, 1933.

29. Sternheimer, R. M., "The Density Effect for the Ionization Loss in Various Materials", *Physical Review*, Vol. 88, No. 4, p. 851, 1952.

30. Birks, J. B., *The Theory and Practice of Scintillation Counting*, Vol. 27 of *International Series of Monographs in Electronics and Instrumentation*, Elsevier Science & Technology Books, Oxford, 2013.

31. Bashkirov, V. A., R. W. Schulte, R. F. Hurley, R. P. Johnson, H. F.-W. Sadrozinski, A. Zatserklyaniy, T. Plautz and V. Giacometti, "Novel Scintillation Detector Design and Performance for Proton Radiography and Computed Tomography", *Medical Physics*, Vol. 43, No. 2, pp. 664–674, 2016.

32. National Nuclear Data Center, "NuDat 3 Database", `https://www.nndc.bnl.gov/nudat3/`, 2025, [Accessed: 2025-05-04].

33. Auger, P., "The Auger Effect", *Surface Science*, Vol. 48, No. 1, pp. 1–8, 1975.

34. Magill, J. and J. Galy, *Radioactivity Radionuclides Radiation*, Springer, Berlin, Germany, 2005 edn., 2004.

35. Yurevich, V. I., "Production of Neutrons in Thick Targets by High-Energy Protons and Nuclei", *Physics of Particles and Nuclei*, Vol. 41, No. 5, pp. 778–825, 2010.

36. Robinson, S. M., D. E. Benker, E. D. Collins, J. G. Ezold, J. R. Garrison and S. L. Hogle, "Production of Cf-252 and Other Transplutonium Isotopes at Oak Ridge National Laboratory", *Radiochimica Acta*, Vol. 108, No. 9, pp. 737–746, 2020.

37. Xin, Y., Q. Pan, L. Wang, B. Xia, Y. Cai, X. Liu and J. Xiong, "Neutron Single-Flow Method for Efficient Production of Cf-252 in High-Flux Fast Reactor", *Nuclear Engineering and Design*, Vol. 430, p. 113680, 2024.

38. Martin, R. C., J. B. Knauer and P. A. Balo, "Production, Distribution and Applications of Californium-252 Neutron Sources", *Applied Radiation and Isotopes*, Vol. 53, No. 4, pp. 785–792, 2000.

39. Pietropaolo, A., M. Angelone, R. Bedogni, N. Colonna, A. N. Hurd, A. Khaplanov, F. Murtas, M. Pillon, E. Schooneveld and M. Tardocchi, "Neutron Detection Techniques from μeV to GeV", *Physics Reports*, Vol. 875, pp. 1–65, 2020.

40. Williams, G. P., "X-Ray Data Booklet", *X-ray Data Booklet*, Vol. 35, p. 52, 2001.

41. Elder, F. R., A. M. Gurewitsch, R. V. Langmuir and H. C. Pollock, "Radiation from Electrons in a Synchrotron", *Physical Review*, Vol. 71, No. 11, pp. 829–830, 1947.

42. Mobilio, S., F. Boscherini, C. Meneghini and others, *Synchrotron Radiation*, Springer, Berlin, 2016.

43. Chadwick, M. B., M. Herman, P. Oblozinský, M. E. Dunn, Y. Danon, A. C. Kahler, D. L. Smith, B. Pritychenko and The ENDF/B-VII.1 Collaboration, "ENDF/B-VII.1 Nuclear Data for Science and Technology: Cross Sections, Covariances, Fission Product Yields and Decay Data", *Nuclear Data Sheets*, Vol. 112, No. 12, pp. 2887–2996, 2011.

44. Wright, A. G., *The Photomultiplier Handbook*, Oxford University Press, Oxford, 2017.

45. Hamamatsu Photonics, "PMT Handbook", `https://www.hamamatsu.com/content/dam/hamamatsu-photonics/sites/documents/99_SALES_LIBRARY/etd/PMT_handbook_v4E.pdf`, 2025, [Accessed: 14-07-2025].

46. Flyckt, S.-O., *Photomultiplier Tubes: Principles and Applications*, Photonis, Brive-la-Gaillarde, France, 2002.

47. Morton, G. A., "The Scintillation Counter Story Part II", *IEEE Transactions on Nuclear Science*, Vol. 22, No. 1, pp. 26–28, 1975.

48. Bondarenko, G., P. Buzhan, B. Dolgoshein, V. Golovin, E. Guschin, A. Ilyin, V. Kaplin, A. Karakash, R. Klanner, V. Pokachalov, E. Popova and K. Smirnov, "Limited Geiger-Mode Microcell Silicon Photodiode: New Results", *Nuclear Instruments and Methods in Physics Research Section A: Accelerators, Spectrometers, Detectors and Associated Equipment*, Vol. 442, No. 1-3, pp. 187–192, 2000.

49. Bonanno, G., P. Finocchiaro, A. Pappalardo, S. Billotta, L. Cosentino, M. Belluso, S. Di Mauro and G. Occhipinti, "Precision Measurements of Photon Detection Efficiency for SiPM Detectors", *Nuclear Instruments and Methods in Physics Research Section A: Accelerators, Spectrometers, Detectors and Associated Equipment*, Vol.

610, No. 1, pp. 93–97, 2009.

50. Derenzo, S. E., M. J. Weber, W. W. Moses and C. Dujardin, "Measurements of the Intrinsic Rise Times of Common Inorganic Scintillators", *IEEE Transactions on Nuclear Science*, Vol. 47, No. 3, pp. 860–864, 2000.

51. Kumar, V. and Z. Luo, "A Review on X-ray Excited Emission Decay Dynamics in Inorganic Scintillator Materials", *Photonics*, Vol. 8, No. 3, p. 71, 2021.

52. Gulick, H., H. Yoneda, T. Takahashi, C. Chen, K. Nakazawa, S. Nagasawa, M. Ando, K. Okuma, A. Joens, S. A. Nussirat and The COSI Collaboration, "A Study of Afterglow Signatures in NaI and CsI Scintillator Modules for the Background and Transient Observer Instrument on COSI", *Nuclear Instruments and Methods in Physics Research Section B: Beam Interactions with Materials and Atoms*, Vol. 561, p. 165631, 2025.

53. JUNO Collaboration, "JUNO Physics and Detector", *Progress in Particle and Nuclear Physics*, Vol. 123, p. 103927, 2022.

54. Decowski, M. P., "KamLAND's Precision Neutrino Oscillation Measurements", *Nuclear Physics B*, Vol. 908, pp. 52–61, 2016.

55. Hamel, M., *Plastic Scintillators*, Springer, Cham, 2021.

56. Forster, T., "10th Spiers Memorial Lecture: Transfer Mechanisms of Electronic Excitation", *Diss. Faraday Soc.*, Vol. 27, pp. 7–17, 1959.

57. Hamel, M., "Progress in Fast and Red Plastic Scintillators", *Chemosensors*, Vol. 10, No. 2, p. 86, 2022.

58. Quaranta, A., S. M. Carturan, T. Marchi, V. L. Kravchuk, F. Gramegna, G. Maggioni and M. Degerlier, "Optical and Scintillation Properties of Polydimethyl-Diphenylsiloxane Based Organic Scintillators", *IEEE Transactions on Nuclear Sci-*

ence, Vol. 57, No. 2, pp. 891–900, 2010.

59. Niedźwiecki, D. M., H. Michalak, M. Kochman, T. Borowicz and A. Czaja, "Evaluation of the Photophysical Properties of Two Scintillators: Crystalline Para-Terphenyl and Plastic-Embedded 2,5-Diphenyloxazole Dye", *The Journal of Physical Chemistry A*, Vol. 126, No. 29, pp. 5273–5283, 2022.

60. Kapłon, Ł. and G. Moskal, "Blue-Emitting Polystyrene Scintillators for Plastic Scintillation Dosimetry", *Bio-Algorithms and Med-Systems*, Vol. 17, No. 3, pp. 191–197, 2021.

61. Kandemir, M. and B. Akgün, "Effects of Polymerization Initiators on Plastic Scintillator Light Output", *Instruments*, Vol. 9, No. 3, p. 19, 2025.

62. Eljen Technology, "EJ-550, EJ-552 - Silicone Grease", `https://eljentechnology.com/products/accessories/ej-550-ej-552`, 2025, [Accessed: 06-11-2025].

63. Leo, W. R., *Techniques for Nuclear and Particle Physics Experiments: A How-to Approach*, Springer Science & Business Media, Berlin, 1994.

64. Frangville, C., A. Grabowski, J. Dumazert, E. Montbarbon, C. Lynde, R. Coulon, A. Venerosy, G. H. V. Bertrand and M. Hamel, "Nanoparticles-Loaded Plastic Scintillators for Fast/Thermal Neutrons/Gamma Discrimination: Simulation and Results", *Nuclear Instruments and Methods in Physics Research Section A: Accelerators, Spectrometers, Detectors and Associated Equipment*, Vol. 942, p. 162370, 2019.

65. Safari, M. J., F. A. Davani and H. Afarideh, "Differentiation Method for Localization of Compton Edge in Organic Scintillation Detectors", *arXiv preprint arXiv:1610.09185*, 2016.

66. ON Semiconductor, "MicroJ Series Datasheet", `https://www.onsemi.com/pdf/`

datasheet/microj-series-d.pdf, 2025, [Accessed: 09-11-2025].

67. Odian, G., *Principles of Polymerization*, John Wiley & Sons, Hoboken, NJ, 2004.

68. Tam, A. K., O. Boyraz, J. Unangst, P. Nazareta, M. Schreuder and M. Nilsson, "Quantum-Dot Doped Polymeric Scintillation Material for Radiation Detection", *Radiation Measurements*, Vol. 111, pp. 27–34, 2018.

69. Sahi, S., W. Chen and K. Jiang, "Luminescence Enhancement of PPO/PVT Scintillators by CeF3 Nanoparticles", *Journal of Luminescence*, Vol. 159, pp. 105–109, 2015.

70. Gosau, J.-M., L. A. Harrah and A. E. Hoyt, "Polysilylene Copolymers for Ultrafast Scintillator Applications. 2. Thin Film Formulations", *Radiation Physics and Chemistry*, Vol. 62, No. 1, pp. 127–132, 2001.

71. Debnath, C., S. Kar, A. K. Agrawal, M. Shukla and S. Verma, "Development of Trans-Stilbene/PMMA Polymer Composites and Their Optical Characterization for Scintillation-Based Imaging and Detector Applications", *IEEE Transactions on Nuclear Science*, Vol. 71, No. 11, pp. 2432–2441, 2024.

72. Serraïma-López, D., M. Guillén, H. Bagán and A. Tarancón, "Scintillation and Structural Properties of Copolymers and Mixtures of Styrene, 9-Vinylcarbazole and 4-Vinylbenzyl Chloride Based Plastic Scintillators", *Applied Radiation and Isotopes*, Vol. 211, p. 111409, 2024.

73. Mahl, A., A. Lim, J. Latta, H. A. Yemam, U. Greife and A. Sellinger, "Methacrylate Based Cross-Linkers for Improved Thermomechanical Properties and Retention of Radiation Detection Response in Plastic Scintillators", *Nuclear Instruments and Methods in Physics Research Section A: Accelerators, Spectrometers, Detectors and Associated Equipment*, Vol. 884, pp. 113–118, 2018.

74. Bedrik, A. I., E. S. Velmozhnaya, P. N. Zhmurin, V. N. Lebedev and V. D. Titskaya,

"Properties of Polystyrene-Based Scintillator with Gadolinium Phenylbutanate", *Inorganic Materials: Applied Research*, Vol. 5, No. 4, pp. 399–402, 2014.

75. Li, W., M. Tao, Y. Li, J. Shi, H. Wu, J. Wang, Z. Wang, G. Ren and Y. Wu, "NaI:Tl,6Li-PVT Composite Scintillator Toward Neutron and Gamma Discrimination", *Radiation Measurements*, Vol. 159, p. 106882, 2022.

76. Almog, Y. and M. Levy, "Effect of Initiator on the Molecular Weight Distribution in Dispersion Polymerization of Styrene", *Journal of Polymer Science: Polymer Chemistry Edition*, Vol. 18, No. 1, pp. 1–11, 1980.

77. Meltzer, T. H. and A. V. Tobolsky, "Kinetics of Polymerization of Styrene Initiated by the System Benzoyl-Peroxide-Dimethylaniline", *Journal of the American Chemical Society*, Vol. 76, No. 20, pp. 5178–5180, 1954.

78. CAEN S.p.A., "DT5790 Technical Information", `https://www.caen.it/products/dt5790/`, 2025, [Accessed: 10-11-2025].

APPENDIX A: LOCATING THE COMPTON EDGE

The Compton edge in a gamma-ray spectrum refers to the region where photons transfer the maximum possible energy through a Compton scattering event within the detector. As this feature does not appear as a sharp peak but rather a gradual drop, the Compton edge value corresponds to the point where the count rate falls to a certain fraction of the Gaussian peak value [64, 65].

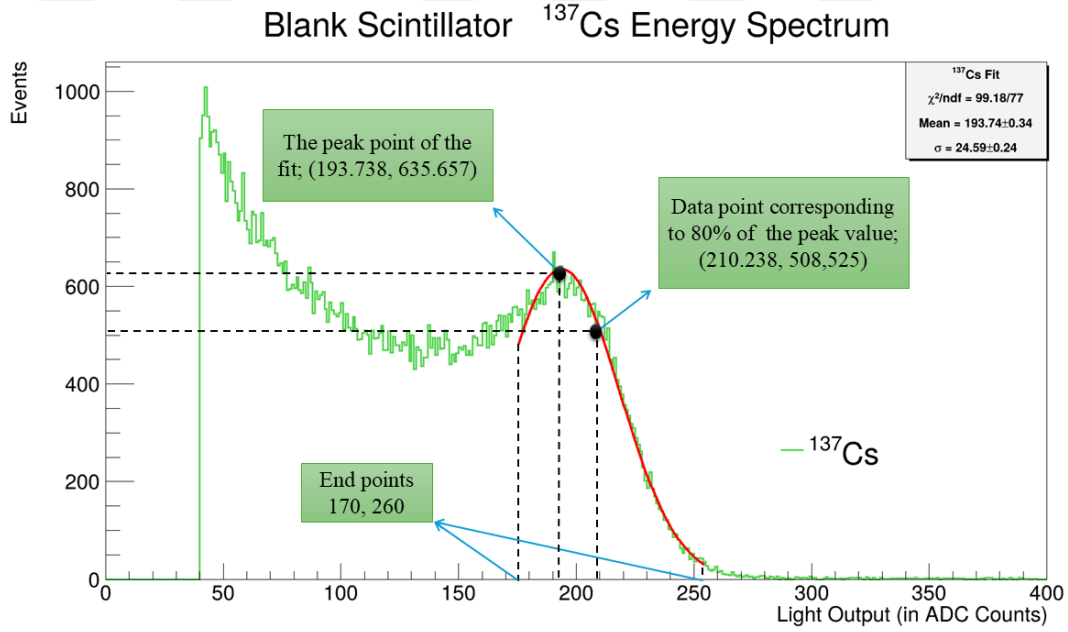

Figure A.1. Blank Scintillator, red line indicates the Gaussian fit to Cs-137 Compton edge.

When a Gaussian fit is applied to an energy spectrum, the following are considered:

- The peak value of the Compton edge part of the spectrum remains inside the chosen fit ranges.

- The fit ranges are chosen such that the χ^2/ndf value is minimized and a ± 5 shift results only in a maximum of 0.6% mean RLY change.
- Once the peak point of the fit is determined, the data point corresponding to 80% of the peak value is located. Therefore, our results are based on raw data, not the fit values.

APPENDIX B: ERROR PROPAGATION

Table 5.3 presents RLY values with uncertainties regarding the fitting procedure. As mentioned in Appendix A, the fit values' ranges are chosen to minimize the χ^2/ndf value to obtain the best fit possible. However, considering any slight misallocation of the Compton edge values, the left end points of the samples are shifted by ± 5 units, and the uncertainties in RLY are calculated.

Let us denote the relevant Compton edge positions, in ADC Counts, as CE_0, CE_{-5}, CE_{+5} for the original fit position, left end points shifted by -5, and left end points shifted by $+5$, respectively. The maximum deviation as a result of these shifts is

$$\sigma_{CE} = max(|CE_0 - CE_{-5}|, |CE_0 - CE_{+5}|). \tag{B.1}$$

Following Equation (3.3), the uncertainty in RLY is calculated as

$$\sigma_{RLY} = RLY_{sample} \times \frac{\sigma_{CE}}{CE_0}. \tag{B.2}$$

The root mean square (RMS) deviation measures the spread of a data set around its average value. It is calculated by taking the differences between each data point and the mean, squaring these differences to avoid cancellation, averaging the squared differences, and finally taking the square root of this average. The mean RLY from measurements at five different energy values for each scintillator was computed. Then, the RMS deviation to quantify the consistency of RLY across these energies was calculated.

The total uncertainties presented in Table 5.3 are obtained by the root sum of squares of the average RLY and RMS errors,

$$\sigma_{Total} = \sqrt{\sigma_{RMS}^2 + \sigma_{average}^2}, \tag{B.3}$$

where $\sigma_{average}$ is calculated by the root sum of squares of σ_{RLY} values divided by the number of Compton edge values N, in this case $N = 5$,

$$\sigma_{average} = \frac{\sqrt{\sum \sigma_{RLY}^2}}{N}. \tag{B.4}$$

APPENDIX C: COPYRIGHTS

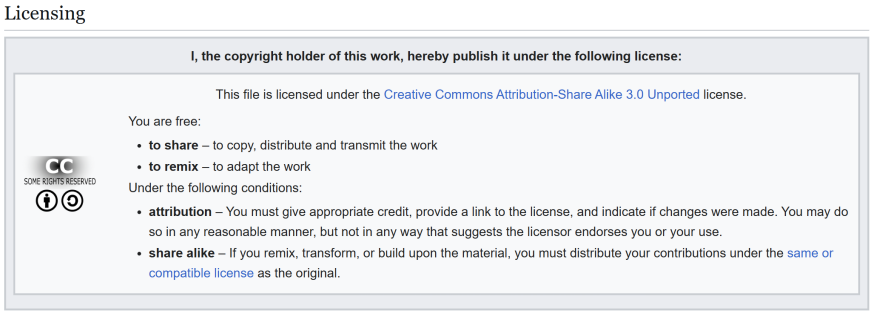
Licensing

I, the copyright holder of this work, hereby publish it under the following license:

This file is licensed under the Creative Commons Attribution-Share Alike 3.0 Unported license.

You are free:

- **to share** – to copy, distribute and transmit the work
- **to remix** – to adapt the work

Under the following conditions:

- **attribution** – You must give appropriate credit, provide a link to the license, and indicate if changes were made. You may do so in any reasonable manner, but not in any way that suggests the licensor endorses you or your use.
- **share alike** – If you remix, transform, or build upon the material, you must distribute your contributions under the same or compatible license as the original.

Figure C.1. Permission for use of Figure 2.7

"Figures 2.1a, 2.2, and 2.5 are adapted from Knoll [23] with permission from John Wiley and Sons. The license terms and conditions are provided below.

Figure 2.6 is adapted from Birks [30] with permission from Elsevier. The license terms and conditions are provided below.

All other figures are the original work of the author.

JOHN WILEY AND SONS LICENSE
TERMS AND CONDITIONS

Dec 25, 2025

This Agreement between Mustafa Kandemir ("You") and John Wiley and Sons ("John Wiley and Sons") consists of your license details and the terms and conditions provided by John Wiley and Sons and Copyright Clearance Center.

License Number	6134140618120
License date	Oct 22, 2025
Licensed Content Publisher	John Wiley and Sons
Licensed Content Publication	Wiley Books
Licensed Content Title	Radiation Detection and Measurement, 4th Edition
Licensed Content Author	Glenn F. Knoll
Licensed Content Date	Aug 1, 2010
Licensed Content Pages	1
Type of use	Dissertation/Thesis
Requestor type	University/Academic
Format	Print and electronic
Portion	Figure/table
Number of figures/tables	3
Will you be translating?	No

Title of new work	Synthesis and Characterization of Plastic Scintillator Samples with Different Additives
Institution name	Bogazici University
Expected presentation date	Dec 2025
Portions	Figure 1.1 Figure 1.5 Figure 8.6
The Requesting Person / Organization to Appear on the License	Mustafa Kandemir
Requestor Location	Mr. Mustafa Kandemir Bogazici University İstanbul, 34342 Turkey
Publisher Tax ID	EU826007151
Total	0.00 USD

Terms and Conditions

TERMS AND CONDITIONS

This copyrighted material is owned by or exclusively licensed to John Wiley & Sons, Inc. or one of its group companies (each a"Wiley Company") or handled on behalf of a society with which a Wiley Company has exclusive publishing rights in relation to a particular work (collectively "WILEY"). By clicking "accept" in connection with completing this licensing transaction, you agree that the following terms and conditions apply to this transaction (along with the billing and payment terms and conditions established by the Copyright Clearance Center Inc., ("CCC's Billing and Payment terms and conditions"), at the time that you opened your RightsLink account (these are available at any time at http://myaccount.copyright.com).

Terms and Conditions

- The materials you have requested permission to reproduce or reuse (the "Wiley Materials") are protected by copyright.
- You are hereby granted a personal, non-exclusive, non-sub licensable (on a stand-alone basis), non-transferable, worldwide, limited license to reproduce the Wiley Materials for the purpose specified in the licensing process. This license, **and any CONTENT (PDF or image file) purchased as part of your order,** is for a one-

time use only and limited to any maximum distribution number specified in the license. The first instance of republication or reuse granted by this license must be completed within two years of the date of the grant of this license (although copies prepared before the end date may be distributed thereafter). The Wiley Materials shall not be used in any other manner or for any other purpose, beyond what is granted in the license. Permission is granted subject to an appropriate acknowledgement given to the author, title of the material/book/journal and the publisher. You shall also duplicate the copyright notice that appears in the Wiley publication in your use of the Wiley Material. Permission is also granted on the understanding that nowhere in the text is a previously published source acknowledged for all or part of this Wiley Material. Any third party content is expressly excluded from this permission.

- With respect to the Wiley Materials, all rights are reserved. Except as expressly granted by the terms of the license, no part of the Wiley Materials may be copied, modified, adapted (except for minor reformatting required by the new Publication), translated, reproduced, transferred or distributed, in any form or by any means, and no derivative works may be made based on the Wiley Materials without the prior permission of the respective copyright owner.**For STM Signatory Publishers clearing permission under the terms of the STM Permissions Guidelines only, the terms of the license are extended to include subsequent editions and for editions in other languages, provided such editions are for the work as a whole in situ and does not involve the separate exploitation of the permitted figures or extracts,** You may not alter, remove or suppress in any manner any copyright, trademark or other notices displayed by the Wiley Materials. You may not license, rent, sell, loan, lease, pledge, offer as security, transfer or assign the Wiley Materials on a stand-alone basis, or any of the rights granted to you hereunder to any other person.

- The Wiley Materials and all of the intellectual property rights therein shall at all times remain the exclusive property of John Wiley & Sons Inc, the Wiley Companies, or their respective licensors, and your interest therein is only that of having possession of and the right to reproduce the Wiley Materials pursuant to Section 2 herein during the continuance of this Agreement. You agree that you own no right, title or interest in or to the Wiley Materials or any of the intellectual property rights therein. You shall have no rights hereunder other than the license as provided for above in Section 2. No right, license or interest to any trademark, trade name, service mark or other branding ("Marks") of WILEY or its licensors is granted hereunder, and you agree that you shall not assert any such right, license or interest with respect thereto

- NEITHER WILEY NOR ITS LICENSORS MAKES ANY WARRANTY OR REPRESENTATION OF ANY KIND TO YOU OR ANY THIRD PARTY, EXPRESS, IMPLIED OR STATUTORY, WITH RESPECT TO THE MATERIALS OR THE ACCURACY OF ANY INFORMATION CONTAINED IN THE MATERIALS, INCLUDING, WITHOUT LIMITATION, ANY IMPLIED WARRANTY OF MERCHANTABILITY, ACCURACY, SATISFACTORY QUALITY, FITNESS FOR A PARTICULAR PURPOSE, USABILITY, INTEGRATION OR NON-INFRINGEMENT AND ALL SUCH WARRANTIES ARE HEREBY EXCLUDED BY WILEY AND ITS LICENSORS AND WAIVED BY YOU.

- WILEY shall have the right to terminate this Agreement immediately upon breach of this Agreement by you.

- You shall indemnify, defend and hold harmless WILEY, its Licensors and their respective directors, officers, agents and employees, from and against any actual or threatened claims, demands, causes of action or proceedings arising from any

breach of this Agreement by you.

- IN NO EVENT SHALL WILEY OR ITS LICENSORS BE LIABLE TO YOU OR ANY OTHER PARTY OR ANY OTHER PERSON OR ENTITY FOR ANY SPECIAL, CONSEQUENTIAL, INCIDENTAL, INDIRECT, EXEMPLARY OR PUNITIVE DAMAGES, HOWEVER CAUSED, ARISING OUT OF OR IN CONNECTION WITH THE DOWNLOADING, PROVISIONING, VIEWING OR USE OF THE MATERIALS REGARDLESS OF THE FORM OF ACTION, WHETHER FOR BREACH OF CONTRACT, BREACH OF WARRANTY, TORT, NEGLIGENCE, INFRINGEMENT OR OTHERWISE (INCLUDING, WITHOUT LIMITATION, DAMAGES BASED ON LOSS OF PROFITS, DATA, FILES, USE, BUSINESS OPPORTUNITY OR CLAIMS OF THIRD PARTIES), AND WHETHER OR NOT THE PARTY HAS BEEN ADVISED OF THE POSSIBILITY OF SUCH DAMAGES. THIS LIMITATION SHALL APPLY NOTWITHSTANDING ANY FAILURE OF ESSENTIAL PURPOSE OF ANY LIMITED REMEDY PROVIDED HEREIN.

- Should any provision of this Agreement be held by a court of competent jurisdiction to be illegal, invalid, or unenforceable, that provision shall be deemed amended to achieve as nearly as possible the same economic effect as the original provision, and the legality, validity and enforceability of the remaining provisions of this Agreement shall not be affected or impaired thereby.

- The failure of either party to enforce any term or condition of this Agreement shall not constitute a waiver of either party's right to enforce each and every term and condition of this Agreement. No breach under this agreement shall be deemed waived or excused by either party unless such waiver or consent is in writing signed by the party granting such waiver or consent. The waiver by or consent of a party to a breach of any provision of this Agreement shall not operate or be construed as a waiver of or consent to any other or subsequent breach by such other party.

- This Agreement may not be assigned (including by operation of law or otherwise) by you without WILEY's prior written consent.

- Any fee required for this permission shall be non-refundable after thirty (30) days from receipt by the CCC.

- These terms and conditions together with CCC's Billing and Payment terms and conditions (which are incorporated herein) form the entire agreement between you and WILEY concerning this licensing transaction and (in the absence of fraud) supersedes all prior agreements and representations of the parties, oral or written. This Agreement may not be amended except in writing signed by both parties. This Agreement shall be binding upon and inure to the benefit of the parties' successors, legal representatives, and authorized assigns.

- In the event of any conflict between your obligations established by these terms and conditions and those established by CCC's Billing and Payment terms and conditions, these terms and conditions shall prevail.

- WILEY expressly reserves all rights not specifically granted in the combination of (i) the license details provided by you and accepted in the course of this licensing transaction, (ii) these terms and conditions and (iii) CCC's Billing and Payment terms and conditions.

- This Agreement will be void if the Type of Use, Format, Circulation, or Requestor Type was misrepresented during the licensing process.

- This Agreement shall be governed by and construed in accordance with the laws of the State of New York, USA, without regards to such state's conflict of law rules. Any legal action, suit or proceeding arising out of or relating to these Terms and Conditions or the breach thereof shall be instituted in a court of competent jurisdiction in New York County in the State of New York in the United States of America and each party hereby consents and submits to the personal jurisdiction of such court, waives any objection to venue in such court and consents to service of process by registered or certified mail, return receipt requested, at the last known address of such party.

WILEY OPEN ACCESS TERMS AND CONDITIONS

Wiley Publishes Open Access Articles in fully Open Access Journals and in Subscription journals offering Online Open. Although most of the fully Open Access journals publish open access articles under the terms of the Creative Commons Attribution (CC BY) License only, the subscription journals and a few of the Open Access Journals offer a choice of Creative Commons Licenses. The license type is clearly identified on the article.

The Creative Commons Attribution License

The Creative Commons Attribution License (CC-BY) allows users to copy, distribute and transmit an article, adapt the article and make commercial use of the article. The CC-BY license permits commercial and non-

Creative Commons Attribution Non-Commercial License

The Creative Commons Attribution Non-Commercial (CC-BY-NC)License permits use, distribution and reproduction in any medium, provided the original work is properly cited and is not used for commercial purposes.(see below)

Creative Commons Attribution-Non-Commercial-NoDerivs License

The Creative Commons Attribution Non-Commercial-NoDerivs License (CC-BY-NC-ND) permits use, distribution and reproduction in any medium, provided the original work is properly cited, is not used for commercial purposes and no modifications or adaptations are made. (see below)

Use by commercial "for-profit" organizations

Use of Wiley Open Access articles for commercial, promotional, or marketing purposes requires further explicit permission from Wiley and will be subject to a fee.

Further details can be found on Wiley Online Library
http://olabout.wiley.com/WileyCDA/Section/id-410895.html

Other Terms and Conditions:

v1.10 Last updated September 2015

Questions? customercare@copyright.com.

ELSEVIER LICENSE
TERMS AND CONDITIONS

Dec 25, 2025

This Agreement between Mustafa Kandemir ("You") and Elsevier ("Elsevier") consists of your license details and the terms and conditions provided by Elsevier and Copyright Clearance Center.

License Number	6175890123885
License date	Dec 25, 2025
Licensed Content Publisher	Elsevier
Licensed Content Publication	Elsevier Books
Licensed Content Title	The Theory and Practice of Scintillation Counting
Licensed Content Author	J.B. BIRKS
Licensed Content Date	Jan 1, 1964
Licensed Content Pages	29
Start Page	39
End Page	67
Type of Use	reuse in a thesis/dissertation
Portion	figures/tables/illustrations
Number of figures/tables/illustrations	2
Format	both print and electronic

Are you the author of this Elsevier chapter?	No
Will you be translating?	No
Title of new work	Synthesis and Characterization of Plastic Scintillator Samples with Different Additives
Institution name	Bogazici University
Expected presentation date	Dec 2025
Portions	Figure 3.7
The Requesting Person / Organization to Appear on the License	Mustafa Kandemir
Requestor Location	Mr. Mustafa Kandemir Bogazici University İstanbul, 34342 Turkey
Publisher Tax ID	GB 494 6272 12
Total	0.00 USD

Terms and Conditions

INTRODUCTION

1. The publisher for this copyrighted material is Elsevier. By clicking "accept" in connection with completing this licensing transaction, you agree that the following terms and conditions apply to this transaction (along with the Billing and Payment terms and conditions established by Copyright Clearance Center, Inc. ("CCC"), at the time that you opened your RightsLink account and that are available at any time at https://myaccount.copyright.com).

GENERAL TERMS

2. Elsevier hereby grants you permission to reproduce the aforementioned material subject to the terms and conditions indicated.

3. Acknowledgement: If any part of the material to be used (for example, figures) has appeared in our publication with credit or acknowledgement to another source, permission

must also be sought from that source. If such permission is not obtained then that material may not be included in your publication/copies. Suitable acknowledgement to the source must be made, either as a footnote or in a reference list at the end of your publication, as follows:

"Reprinted from Publication title, Vol /edition number, Author(s), Title of article / title of chapter, Pages No., Copyright (Year), with permission from Elsevier [OR APPLICABLE SOCIETY COPYRIGHT OWNER]." Also Lancet special credit - "Reprinted from The Lancet, Vol. number, Author(s), Title of article, Pages No., Copyright (Year), with permission from Elsevier."

4. Reproduction of this material is confined to the purpose and/or media for which permission is hereby given. The material may not be reproduced or used in any other way, including use in combination with an artificial intelligence tool (including to train an algorithm, test, process, analyse, generate output and/or develop any form of artificial intelligence tool), or to create any derivative work and/or service (including resulting from the use of artificial intelligence tools).

5. Altering/Modifying Material: Not Permitted. However figures and illustrations may be altered/adapted minimally to serve your work. Any other abbreviations, additions, deletions and/or any other alterations shall be made only with prior written authorization of Elsevier Ltd. (Please contact Elsevier's permissions helpdesk here). No modifications can be made to any Lancet figures/tables and they must be reproduced in full.

6. If the permission fee for the requested use of our material is waived in this instance, please be advised that your future requests for Elsevier materials may attract a fee.

7. Reservation of Rights: Publisher reserves all rights not specifically granted in the combination of (i) the license details provided by you and accepted in the course of this licensing transaction, (ii) these terms and conditions and (iii) CCC's Billing and Payment terms and conditions.

8. License Contingent Upon Payment: While you may exercise the rights licensed immediately upon issuance of the license at the end of the licensing process for the transaction, provided that you have disclosed complete and accurate details of your proposed use, no license is finally effective unless and until full payment is received from you (either by publisher or by CCC) as provided in CCC's Billing and Payment terms and conditions. If full payment is not received on a timely basis, then any license preliminarily granted shall be deemed automatically revoked and shall be void as if never granted. Further, in the event that you breach any of these terms and conditions or any of CCC's Billing and Payment terms and conditions, the license is automatically revoked and shall be void as if never granted. Use of materials as described in a revoked license, as well as any use of the materials beyond the scope of an unrevoked license, may constitute copyright infringement and publisher reserves the right to take any and all action to protect its copyright in the materials.

9. Warranties: Publisher makes no representations or warranties with respect to the licensed material.

10. Indemnity: You hereby indemnify and agree to hold harmless publisher and CCC, and their respective officers, directors, employees and agents, from and against any and all claims arising out of your use of the licensed material other than as specifically authorized pursuant to this license.

11. No Transfer of License: This license is personal to you and may not be sublicensed, assigned, or transferred by you to any other person without publisher's written permission.

12. No Amendment Except in Writing: This license may not be amended except in a writing signed by both parties (or, in the case of publisher, by CCC on publisher's behalf).

13. Objection to Contrary Terms: Publisher hereby objects to any terms contained in any purchase order, acknowledgment, check endorsement or other writing prepared by you, which terms are inconsistent with these terms and conditions or CCC's Billing and Payment terms and conditions. These terms and conditions, together with CCC's Billing and Payment terms and conditions (which are incorporated herein), comprise the entire agreement between you and publisher (and CCC) concerning this licensing transaction. In the event of any conflict between your obligations established by these terms and conditions and those established by CCC's Billing and Payment terms and conditions, these terms and conditions shall control.

14. Revocation: Elsevier or Copyright Clearance Center may deny the permissions described in this License at their sole discretion, for any reason or no reason, with a full refund payable to you. Notice of such denial will be made using the contact information provided by you. Failure to receive such notice will not alter or invalidate the denial. In no event will Elsevier or Copyright Clearance Center be responsible or liable for any costs, expenses or damage incurred by you as a result of a denial of your permission request, other than a refund of the amount(s) paid by you to Elsevier and/or Copyright Clearance Center for denied permissions.

LIMITED LICENSE

The following terms and conditions apply only to specific license types:

15. **Translation**: This permission is granted for non-exclusive world **English** rights only unless your license was granted for translation rights. If you licensed translation rights you may only translate this content into the languages you requested. A professional translator must perform all translations and reproduce the content word for word preserving the integrity of the article.

16. **Posting licensed content on any Website**: The following terms and conditions apply as follows: Licensing material from an Elsevier journal: All content posted to the web site must maintain the copyright information line on the bottom of each image; A hyper-text must be included to the Homepage of the journal from which you are licensing at http://www.sciencedirect.com/science/journal/xxxxx or the Elsevier homepage for books at http://www.elsevier.com; Central Storage: This license does not include permission for a scanned version of the material to be stored in a central repository such as that provided by Heron/XanEdu.

Licensing material from an Elsevier book: A hyper-text link must be included to the Elsevier homepage at http://www.elsevier.com . All content posted to the web site must maintain the copyright information line on the bottom of each image.

Posting licensed content on Electronic reserve: In addition to the above the following clauses are applicable: The web site must be password-protected and made available only to bona fide students registered on a relevant course. This permission is granted for 1 year only. You may obtain a new license for future website posting.

17. **For journal authors:** the following clauses are applicable in addition to the above:

Preprints:

A preprint is an author's own write-up of research results and analysis, it has not been peer-reviewed, nor has it had any other value added to it by a publisher (such as formatting, copyright, technical enhancement etc.).

Authors can share their preprints anywhere at any time. Preprints should not be added to or enhanced in any way in order to appear more like, or to substitute for, the final versions

of articles however authors can update their preprints on arXiv or RePEc with their Accepted Author Manuscript (see below).

If accepted for publication, we encourage authors to link from the preprint to their formal publication via its DOI. Millions of researchers have access to the formal publications on ScienceDirect, and so links will help users to find, access, cite and use the best available version. Please note that Cell Press, The Lancet and some society-owned have different preprint policies. Information on these policies is available on the journal homepage.

Accepted Author Manuscripts: An accepted author manuscript is the manuscript of an article that has been accepted for publication and which typically includes author-incorporated changes suggested during submission, peer review and editor-author communications.

Authors can share their accepted author manuscript:

- immediately
    - via their non-commercial person homepage or blog
    - by updating a preprint in arXiv or RePEc with the accepted manuscript
    - via their research institute or institutional repository for internal institutional uses or as part of an invitation-only research collaboration work-group
    - directly by providing copies to their students or to research collaborators for their personal use
    - for private scholarly sharing as part of an invitation-only work group on commercial sites with which Elsevier has an agreement
- After the embargo period
    - via non-commercial hosting platforms such as their institutional repository
    - via commercial sites with which Elsevier has an agreement

In all cases accepted manuscripts should:

- link to the formal publication via its DOI
- bear a CC-BY-NC-ND license - this is easy to do
- if aggregated with other manuscripts, for example in a repository or other site, be shared in alignment with our hosting policy not be added to or enhanced in any way to appear more like, or to substitute for, the published journal article.

Published journal article (JPA): A published journal article (PJA) is the definitive final record of published research that appears or will appear in the journal and embodies all value-adding publishing activities including peer review co-ordination, copy-editing, formatting, (if relevant) pagination and online enrichment.

Policies for sharing publishing journal articles differ for subscription and gold open access articles:

Subscription Articles: If you are an author, please share a link to your article rather than the full-text. Millions of researchers have access to the formal publications on ScienceDirect, and so links will help your users to find, access, cite, and use the best available version.

Theses and dissertations which contain embedded PJAs as part of the formal submission can be posted publicly by the awarding institution with DOI links back to the formal publications on ScienceDirect.

If you are affiliated with a library that subscribes to ScienceDirect you have additional private sharing rights for others' research accessed under that agreement. This includes use for classroom teaching and internal training at the institution (including use in course packs and courseware programs), and inclusion of the article for grant funding purposes.

Gold Open Access Articles: May be shared according to the author-selected end-user license and should contain a CrossMark logo, the end user license, and a DOI link to the formal publication on ScienceDirect.

Please refer to Elsevier's posting policy for further information.

18. **For book authors** the following clauses are applicable in addition to the above: Authors are permitted to place a brief summary of their work online only. You are not allowed to download and post the published electronic version of your chapter, nor may you scan the printed edition to create an electronic version. **Posting to a repository:** Authors are permitted to post a summary of their chapter only in their institution's repository.

19. **Thesis/Dissertation**: If your license is for use in a thesis/dissertation your thesis may be submitted to your institution in either print or electronic form. Should your thesis be published commercially, please reapply for permission. These requirements include permission for the Library and Archives of Canada to supply single copies, on demand, of the complete thesis and include permission for Proquest/UMI to supply single copies, on demand, of the complete thesis. Should your thesis be published commercially, please reapply for permission. Theses and dissertations which contain embedded PJAs as part of the formal submission can be posted publicly by the awarding institution with DOI links back to the formal publications on ScienceDirect.

Elsevier Open Access Terms and Conditions

You can publish open access with Elsevier in hundreds of open access journals or in nearly 2000 established subscription journals that support open access publishing. Permitted third party re-use of these open access articles is defined by the author's choice of Creative Commons user license. See our open access license policy for more information.

Terms & Conditions applicable to all Open Access articles published with Elsevier:

Any reuse of the article must not represent the author as endorsing the adaptation of the article nor should the article be modified in such a way as to damage the author's honour or reputation. If any changes have been made, such changes must be clearly indicated.

The author(s) must be appropriately credited and we ask that you include the end user license and a DOI link to the formal publication on ScienceDirect.

If any part of the material to be used (for example, figures) has appeared in our publication with credit or acknowledgement to another source it is the responsibility of the user to ensure their reuse complies with the terms and conditions determined by the rights holder.

Additional Terms & Conditions applicable to each Creative Commons user license:

CC BY: The CC-BY license allows users to copy, to create extracts, abstracts and new works from the Article, to alter and revise the Article and to make commercial use of the Article (including reuse and/or resale of the Article by commercial entities), provided the user gives appropriate credit (with a link to the formal publication through the relevant DOI), provides a link to the license, indicates if changes were made and the licensor is not represented as endorsing the use made of the work. The full details of the license are available at http://creativecommons.org/licenses/by/4.0.

CC BY NC SA: The CC BY-NC-SA license allows users to copy, to create extracts, abstracts and new works from the Article, to alter and revise the Article, provided this is